

This is an Open Access document downloaded from ORCA, Cardiff University's institutional repository: <https://orca.cardiff.ac.uk/id/eprint/111179/>

This is the author's version of a work that was submitted to / accepted for publication.

Citation for final published version:

Gray, William R., Rae, James W. B., Wills, Robert C. J., Shevenell, Amelia E., Taylor, Ben, Burke, Andrea, Foster, Gavin L. and Lear, Caroline H. 2018. Deglacial upwelling, productivity and CO<sub>2</sub> outgassing in the North Pacific Ocean. *Nature Geoscience* 11 , pp. 340-344. 10.1038/s41561-018-0108-6

Publishers page: <http://dx.doi.org/10.1038/s41561-018-0108-6>

Please note:

Changes made as a result of publishing processes such as copy-editing, formatting and page numbers may not be reflected in this version. For the definitive version of this publication, please refer to the published source. You are advised to consult the publisher's version if you wish to cite this paper.

This version is being made available in accordance with publisher policies. See <http://orca.cf.ac.uk/policies.html> for usage policies. Copyright and moral rights for publications made available in ORCA are retained by the copyright holders.



# **Deglacial upwelling, productivity and CO<sub>2</sub> outgassing in the North Pacific Ocean**

William R Gray<sup>1,2</sup>, James W B Rae<sup>2</sup>, Robert C J Wills<sup>3</sup>, Amelia E Shevenell<sup>4,5</sup>,  
Ben Taylor<sup>2</sup>, Andrea Burke<sup>2</sup>, Gavin L Foster<sup>6</sup>, Caroline H Lear<sup>7</sup>

<sup>1</sup>Department of Geography, University College London, UK

<sup>2</sup>School of Earth and Environmental Sciences, University of St Andrews, UK

<sup>3</sup>Department of Atmospheric Sciences, University of Washington, Seattle, WA,  
USA

<sup>4</sup>Department of Earth Sciences, University College London, UK

<sup>5</sup>College of Marine Science, University of South Florida, Tampa, FL, USA

<sup>6</sup>Ocean and Earth Science, National Oceanography Centre Southampton,  
University of Southampton, UK

<sup>7</sup>School of Earth and Ocean Sciences, Cardiff University, UK

**The interplay between ocean circulation and biological productivity affects atmospheric CO<sub>2</sub> levels and marine oxygen concentrations. During the warming of the last deglaciation, the North Pacific experienced a peak in productivity and widespread hypoxia, with changes in circulation, iron supply, and light limitation all proposed as potential drivers. Here we use the boron-isotope composition of planktic foraminifera from a sediment core in the western North Pacific to reconstruct pH and dissolved CO<sub>2</sub> concentrations from 24,000 to 8,000 years ago. We find that the productivity peak during the Bølling-Allerød warm interval, 14,700 to 12,900 years ago, was associated with a**

27 **decrease in near-surface pH and an increase in  $p\text{CO}_2$ , and must**  
28 **therefore have been driven by increased supply of nutrient and  $\text{CO}_2$ -rich**  
29 **waters. In a climate model ensemble (PMIP3), the presence of large ice**  
30 **sheets over North America results in high rates of wind-driven upwelling**  
31 **within the subpolar North Pacific. We suggest that this process,**  
32 **combined with collapse of North Pacific Intermediate Water formation at**  
33 **the onset of the Bølling-Allerød, led to high rates of upwelling of water**  
34 **rich in nutrients and  $\text{CO}_2$ , and supported the peak in productivity. The**  
35 **respiration of this organic matter, along with poor ventilation, likely**  
36 **caused the regional hypoxia. We suggest that  $\text{CO}_2$  outgassing from the**  
37 **North Pacific helped to maintain high atmospheric  $\text{CO}_2$  concentrations**  
38 **during the Bølling-Allerød and contributed to the deglacial  $\text{CO}_2$  rise.**

39

40 The balance between the supply of nutrients and carbon to surface waters via  
41 ocean circulation and their removal via biological productivity is a first order  
42 control on atmospheric  $\text{CO}_2$ . This is particularly important at high latitudes<sup>1,2</sup>,  
43 where Ekman suction, driven by cyclonic wind stress, and winter mixing  
44 supply  $\text{CO}_2$  from the deep ocean to the surface. Depending on the availability  
45 of light and micronutrients, such as iron, this  $\text{CO}_2$  may be captured by  
46 photosynthesis and returned to the deep ocean (the “biological pump”), or  
47 may escape to the atmosphere. The balance between circulation and  
48 biological productivity is also crucial for determining the ocean’s dissolved  
49 oxygen content. Ventilation of the ocean at high latitudes mixes oxygen-rich  
50 waters from the surface into the ocean’s interior, where oxygen is consumed

51 by the respiration of sinking organic matter, coupling the biogeochemical  
52 cycles of oxygen and carbon.

53

54 Dramatic changes in these biogeochemical balances are thought to occur  
55 during Pleistocene deglaciations, with reorganisations of circulation and  
56 productivity at high latitudes leading to changes in oceanic oxygen content  
57 and rapid atmospheric CO<sub>2</sub> rise<sup>1-4</sup>. However, the degree to which these  
58 changes in CO<sub>2</sub> and oxygen are driven by circulation versus biological  
59 productivity remains unknown, limiting our understanding of the mechanisms  
60 driving glacial-interglacial variations in CO<sub>2</sub> and climate. Particularly enigmatic  
61 are the dramatic peaks in productivity observed throughout the North Pacific  
62 Ocean during every deglaciation of at least the last ~1 Ma<sup>5-8</sup>. During the  
63 Bølling-Allerød interval (14.7-12.9 ka) of the last deglaciation (the only  
64 deglaciation for which we currently have records of intermediate-ocean redox)  
65 the productivity maximum is associated with widespread intermediate-ocean  
66 hypoxia in the North Pacific<sup>3,9-11</sup>. Since the discovery of these events more  
67 than 25 years ago<sup>5,10</sup> multiple explanations have been put forward, yet there is  
68 no consensus on the cause of either the productivity or the hypoxia; indeed  
69 the degree to which the productivity and hypoxia are linked, and even the  
70 direction of causation, are still contested. Some studies have proposed the  
71 productivity maximum was caused by an increase in the supply of nutrient and  
72 carbon rich waters<sup>7,12</sup>, while others have suggested alleviation of iron<sup>11,13</sup>  
73 and/or light limitation as the main driver<sup>14</sup>. Early work debated the dominance  
74 of reduced ventilation versus increased productivity as the primary cause of  
75 the hypoxia<sup>9,10</sup>, while more recently it has been proposed that hypoxia was

76 initially induced by subsurface warming, and that iron release from hypoxic  
77 sediments drove the increase in productivity<sup>11</sup>.

78

79 Given the large reservoir of dissolved inorganic carbon (DIC) in the North  
80 Pacific interior<sup>15</sup> (Figure 1), a change in its supply and removal to and from the  
81 surface could have significant impact on the global carbon cycle, and play a  
82 role in glacial termination. Understanding the nature of these events is also  
83 important as they have been suggested to provide insights in to future  
84 changes in hypoxia and productivity in a rapidly warming climate<sup>3,11</sup>.

85

#### 86 **Boron isotopes and CO<sub>2</sub> supply**

87

88 To determine the cause of the Bølling-Allerød productivity maximum, we  
89 measured the boron isotope composition ( $\delta^{11}\text{B}$ ) of the planktic foraminifera *N.*  
90 *pachyderma* from deglacial sediments in core MD01-2416 (51.27°N,  
91 167.73°E, 2317 m water depth) (Methods). The core site is located close to  
92 the center of the high nutrient and CO<sub>2</sub> pool in the modern subpolar North  
93 Pacific (Figure 1), making it ideally suited to track changes in the  
94 biogeochemistry of the region.  $\delta^{11}\text{B}$  is a proxy for seawater pH, which tracks  
95 seawater CO<sub>2</sub> chemistry, and with an estimate of one other parameter of the  
96 carbonate system (here alkalinity), allows the quantification of the CO<sub>2</sub>  
97 concentration of past seawater<sup>16</sup> (Methods).

98

99 Our results show a general decrease in near-surface pH over deglaciation,  
100 with a glacial high of  $8.31 \pm 0.04$  ( $1\sigma$ ) falling to a value of  $8.14 \pm 0.04$  in the early

101 Holocene, identical to pre-industrial pH at 50m water depth<sup>15</sup> (Figure 2).  
102 Punctuating the general decline in pH is a pronounced pH minimum of  
103  $8.07\pm 0.05$  in the early Bølling-Allerød, coeval with the maximum in  
104 productivity. At this time,  $p\text{CO}_2$  in the near surface ocean reached a maximum  
105 of  $373\pm 46$   $\mu\text{atm}$  ( $1\sigma$ ) (Figure 3). The decrease in pH and increase in  $\text{CO}_2$   
106 demonstrates that the supply of carbon and nutrients to the surface ocean  
107 was greater than their removal by export production (Supplementary Figure  
108 1). As export production during the Bølling-Allerød was higher than today<sup>6,19</sup>,  
109 it follows that the supply of carbon and macronutrients must also have been  
110 higher.

111

### 112 **PMIP3 model ensemble and paleo-circulation tracers**

113

114 To investigate the physical mechanisms underlying the increase in nutrient  
115 and  $\text{CO}_2$  supply, we looked for large-scale changes in the PMIP3 model  
116 ensemble<sup>31</sup> under glacial boundary conditions, alongside paleo-tracers of  
117 ocean circulation. Although formation of North Pacific Intermediate Water  
118 (NPIW) is extremely limited today<sup>32</sup>, overturning circulation within the basin  
119 was significantly enhanced during the last glacial maximum (LGM): benthic  
120 foraminiferal  $\delta^{13}\text{C}$  records indicate glacial expansion of NPIW to depths of  
121  $>1500$  m<sup>29,33,34</sup> (Supplementary Figure 2), flushing nutrients and carbon from  
122 intermediate waters and deepening the interior ocean nutrient/carbon  
123 reservoir. North Pacific ventilation may have been even deeper and more  
124 vigorous during early deglaciation<sup>28,30,35</sup>, with possible localised deepwater  
125 formation during Heinrich Stadial 1<sup>30,35,36</sup> (HS1) potentially driving the early-

126 deglacial decrease in pH observed in our record (Methods). However, at the  
127 onset of the Bølling-Allerød a rapid decrease in benthic  $\delta^{13}\text{C}$  and increase in  
128 benthic radiocarbon ages indicate a collapse in NPIW formation<sup>28,30</sup>, and a  
129 circulation more similar to the modern<sup>36</sup> (Figure 3 and Supplementary Figure  
130 3).

131

132 If the Bølling-Allerød was characterised by similar overturning circulation to  
133 today, why was the supply of nutrients and carbon to the surface ocean so  
134 much higher? All eight models in the PMIP3 ensemble show substantial  
135 increase in wind stress curl within the subpolar gyre under glacial boundary  
136 conditions, with an ensemble mean increase of ~60% relative to pre-industrial  
137 (Figure 4). This is driven by the presence of an ice sheet over North America,  
138 which causes a strengthening of the westerlies and a southward shift in the  
139 polar easterlies, substantially increasing meridional wind shear and  
140 associated upwelling by Ekman suction within the subpolar gyre.

141

142 At the onset of the Bølling-Allerød large ice sheets remained over North  
143 America, with the Laurentide Ice Sheet having lost only ~15% of its mass<sup>37</sup>.  
144 Ekman suction within the subpolar gyre would therefore have been  
145 significantly higher than modern. During the LGM, nutrient flushing by  
146 enhanced NPIW formation would have prevented the increase in Ekman  
147 suction from increasing the nutrient/carbon supply. However, following the  
148 collapse in NPIW at the onset of the Bølling-Allerød, the interior ocean  
149 nutrient/carbon reservoir would have shoaled, becoming accessible to the  
150 surface ocean (Supplementary Figure 3). This combination of nutrient- and

151 carbon- rich subsurface waters and enhanced Ekman suction led to a  
152 substantial increase in nutrient and carbon supply to the surface.

153

#### 154 **Nutrient utilisation and hypoxia**

155

156 Higher iron availability from atmospheric dust flux and the alleviation of light-  
157 limitation in warm seasonally-stratified waters would have also helped Bølling-  
158 Allerød productivity to exceed present-day levels<sup>14,27</sup> (Methods). However, our  
159 pH and CO<sub>2</sub> record demonstrates that carbon and nutrient supply  
160 overwhelmed iron and light availability, leaving a significantly higher  
161 proportion of the upwelled macronutrients and carbon unutilised, and reducing  
162 the net efficiency of the biological pump at this location. In contrast to  $\delta^{11}\text{B}$ ,  
163 foraminiferal  $\delta^{15}\text{N}$  shows little change at the onset of the Bølling-Allerød  
164 productivity maximum<sup>19,22,25</sup> (Figure 2). While no change in  $\delta^{15}\text{N}$  during an  
165 increase in productivity is consistent with an increase in nutrient supply<sup>19</sup>,  
166 previous interpretations have suggested increased nutrient supply was  
167 balanced by higher export production, such that there was no net change in  
168 the efficiency of the biological pump<sup>19</sup>. However,  $\delta^{15}\text{N}$  is also influenced by the  
169 isotopic composition of source water nitrate, which is thought to have  
170 increased at the Bølling-Allerød due to enhanced denitrification associated  
171 with regional hypoxia<sup>22,25,26,38</sup> (Figure 2). Signals of reduced nutrient  
172 utilisation at the Bølling-Allerød are thus likely to be somewhat masked or  
173 delayed in  $\delta^{15}\text{N}$  records (Methods).

174



175 The increase in export production during the Bølling-Allerød would have  
176 increased organic matter respiration, consuming oxygen in the ocean's  
177 interior. The supply of oxygen to intermediate waters would also have been  
178 reduced, due to the collapse in NPIW formation. Both processes thus  
179 contributed to the regional hypoxia observed at this time. The initiation of  
180 hypoxia may have acted as a positive feedback on productivity by increasing  
181 iron concentrations within upwelling waters<sup>11</sup>, but it was not the primary cause  
182 of the increase in productivity.

183

#### 184 **Deglacial CO<sub>2</sub> rise**

185

186 The increase in  $p\text{CO}_2$  within the near-surface ocean at the onset of the  
187 Bølling-Allerød would have resulted in significant outgassing of  $\text{CO}_2$ , with our  
188 reconstructed ocean-atmosphere  $p\text{CO}_2$  difference being  $\sim 130 \mu\text{atm}$ . Although  
189 *N. pachyderma* calcifies at around  $\sim 50$  m water depth (Methods) the average  
190 annual  $p\text{CO}_2$  difference between 50m depth and the surface ocean is only  
191  $\sim 10 \mu\text{atm}$  at the core site today, thus the surface ocean would have also  
192 experienced elevated levels of  $\text{CO}_2$  (Methods). A significant release of  $\text{CO}_2$  is  
193 also supported by the warm temperatures recorded by the Mg/Ca of *N.*  
194 *pachyderma* during this time (Figure 3), which, as well as indicating a  
195 relatively near-surface habitat, would also have helped drive  $\text{CO}_2$  outgassing  
196 from the ocean to atmosphere (Methods). Release of  $\text{CO}_2$  from the subpolar  
197 Pacific at the onset of the Bølling-Allerød may have contributed to the rapid  
198  $\sim 10 \mu\text{atm}$  increase in atmospheric  $\text{CO}_2$  observed at this time<sup>4,12</sup> (Figure 3;  
199 Methods). Furthermore, continued  $\text{CO}_2$  outgassing from the North Pacific

200 would have maintained the high levels of atmospheric  $p\text{CO}_2$  observed  
201 throughout the Bølling-Allerød, countering the return to more stratified  
202 conditions in the Southern Ocean<sup>4,16,39,40</sup> and the ventilation of the Atlantic  
203 with low-preformed nutrient NADW<sup>41</sup>, both of which should drive down  
204 atmospheric  $p\text{CO}_2$ . The upwelling of  $\text{CO}_2$ -rich waters in the North Pacific may  
205 thus allow atmospheric  $p\text{CO}_2$  to stay high – rather than falling – during the  
206 Bølling-Allerød, and help drive continued deglaciation.

207

208 Results from ocean drilling in the Bering Sea indicate an expansion of NPIW  
209 during every glacial period of the last 1.2 million years<sup>42</sup>. All that is required  
210 for the model proposed here to explain the regular deglacial North Pacific  
211 productivity peaks is that the switch from the enhanced glacial mode of NPIW  
212 formation to the reduced interglacial mode precedes the loss of the Laurentide  
213 Ice Sheet and its associated enhanced Ekman suction. Brine rejection within  
214 the Bering Sea has been suggested as an important process by which NPIW  
215 formation was enhanced during glacial periods<sup>42</sup>. Over the last deglaciation  
216 there was an almost total loss of sea ice within the Bering Sea following the  
217 Northern Hemisphere warming at the Bølling-Allerød<sup>43</sup>, however the  
218 Laurentide Ice Sheet did not ablate completely until ~7000 years later<sup>37</sup>. If the  
219 expansion of NPIW during glacial periods is driven by enhanced brine  
220 rejection, then the loss of sea ice prior to ice sheets during deglacial warming  
221 would dictate that increased upwelling of carbon and nutrient rich waters –  
222 and associated  $\text{CO}_2$  release – would regularly occur during glacial  
223 terminations.

224

225 **References**

- 226 1. Toggweiler, J. R. Variation of Atmospheric CO<sub>2</sub> by Ventilation of the  
227 Ocean's Deepest Water. *Paleoceanography* **14**, 571–588 (1999).
- 228 2. Sigman, D. M., Hain, M. P. & Haug, G. H. The polar ocean and glacial  
229 cycles in atmospheric CO<sub>2</sub> concentration. *Nature* **466**, 47–55 (2010).
- 230 3. Jaccard, S. L. & Galbraith, E. D. Large climate-driven changes of  
231 oceanic oxygen concentrations during the last deglaciation. *Nature*  
232 *Geoscience* **5**, 151–156 (2011).
- 233 4. Marcott, S. A. *et al.* Centennial-scale changes in the global carbon cycle  
234 during the last deglaciation. *Nature* **514**, 616–619 (2014).
- 235 5. Keigwin, L., Jones, G. A. & Froelich, P. N. A 15,000 year  
236 paleoenvironmental record from Meiji Seamount, far northwestern  
237 Pacific. *Earth and Planetary Science Letters* **111**, 425–440 (1992).
- 238 6. Kohfeld, K. E. & Chase, Z. Controls on deglacial changes in biogenic  
239 fluxes in the North Pacific Ocean. *Quaternary Science Reviews* **30**,  
240 3350–3363 (2011).
- 241 7. Jaccard, S. L. *et al.* Glacial/interglacial changes in subarctic North  
242 Pacific stratification. *Science* **308**, 1003–1006 (2005).
- 243 8. Jaccard, S. L., Galbraith, E. D., Sigman, D. M. & Haug, G. H. A  
244 pervasive link between Antarctic ice core and subarctic Pacific sediment  
245 records over the past 800kyrs. *Quaternary Science Reviews* **29**, 206–  
246 212 (2010).
- 247 9. Crusius, J., Pedersen, T. F., Kienast, S., Keigwin, L. & Labeyrie, L.  
248 Influence of northwest Pacific productivity on North Pacific Intermediate  
249 Water oxygen concentrations during the Bølling-Ållerød interval (14.7–

- 250 12.9 ka). *Geol* **32**, 633–636 (2004).
- 251 10. Behl, R. J. & Kennett, J. P. Brief interstadial events in the Santa  
252 Barbara basin, NE Pacific, during the past 60 kyr. *Nature* **379**, 243–245  
253 (1996).
- 254 11. Praetorius, S. K. *et al.* North Pacific deglacial hypoxic events linked to  
255 abrupt ocean warming. *Nature* **527**, 362–366 (2015).
- 256 12. Galbraith, E. D. *et al.* Carbon dioxide release from the North Pacific  
257 abyss during the last deglaciation. *Nature* **449**, 890–893 (2007).
- 258 13. Mix, A. C. *et al.* in *Mechanisms of Global Climate Change at Millennial*  
259 *Time Scales* (eds. Clark, P. U., Webb, R. S. & Keigwin, L.) (American  
260 Geophysical Union, 1999). doi:10.1029/GM112p0127
- 261 14. Lam, P. J. *et al.* Transient stratification as the cause of the North Pacific  
262 productivity spike during deglaciation. *Nature Geoscience* **6**, 622–626  
263 (2013).
- 264 15. Key, R. M., Olsen, A., van Heuven, S. & Lauvset, S. K. Global Ocean  
265 Data Analysis Project, Version 2 (GLODAPv2). *ORNL/CDIAC-162*  
266 (2015). doi:10.3334/CDIAC/OTG
- 267 16. Martínez-Botí, M. A. *et al.* Boron isotope evidence for oceanic carbon  
268 dioxide leakage during the last deglaciation. *Nature* **518**, 219–222  
269 (2015).
- 270 17. Takahashi, T. *et al.* Climatological mean and decadal change in surface  
271 ocean  $p\text{CO}_2$ , and net sea–air  $\text{CO}_2$  flux over the global oceans. *Deep*  
272 *Sea Research Part II: Topical Studies in Oceanography* **56**, 554–577  
273 (2009).
- 274 18. Boyer, T. P. *et al.* *World Ocean Database 2013. NOAA Atlas NESDIS*

- 275           **72**, 209 (2013).
- 276 19. Ren, H. *et al.* Glacial-to-interglacial changes in nitrate supply and  
277 consumption in the subarctic North Pacific from microfossil-bound N  
278 isotopes at two trophic levels. *Paleoceanography* **30**, 1217–1232  
279 (2015).
- 280 20. Key, R. M. *et al.* A global ocean carbon climatology: Results from  
281 Global Data Analysis Project (GLODAP). *Global Biogeochem. Cycles*  
282 **18**, GB4031 (2004).
- 283 21. Gebhardt, H. *et al.* Paleonutrient and productivity records from the  
284 subarctic North Pacific for Pleistocene glacial terminations I to V.  
285 *Paleoceanography* **23**, PA4212 (2008).
- 286 22. Brunelle, B. G. *et al.* Glacial/interglacial changes in nutrient supply and  
287 stratification in the western subarctic North Pacific since the penultimate  
288 glacial maximum. *Quaternary Science Reviews* **29**, 2579–2590 (2010).
- 289 23. Jaccard, S. L. *et al.* Subarctic Pacific evidence for a glacial deepening  
290 of the oceanic respired carbon pool. *Earth and Planetary Science*  
291 *Letters* **277**, 156–165 (2009).
- 292 24. Barron, J. A., Bukry, D., Dean, W. E., Addison, J. A. & Finney, B.  
293 Paleoceanography of the Gulf of Alaska during the past 15,000 years:  
294 Results from diatoms, silicoflagellates, and geochemistry. *Marine*  
295 *Micropaleontology* **72**, 176–195 (2009).
- 296 25. Galbraith, E. D. *et al.* Consistent relationship between global climate  
297 and surface nitrate utilization in the western subarctic Pacific throughout  
298 the last 500 ka. *Paleoceanography* **23**, PA2212 (2008).

- 299 26. Hendy, I. L., Pedersen, T. F., Kennett, J. P. & Tada, R. Intermittent  
300 existence of a southern Californian upwelling cell during submillennial  
301 climate change of the last 60 kyr. *Paleoceanography* **19**, PA3007  
302 (2004).
- 303 27. Serno, S. *et al.* Comparing dust flux records from the Subarctic North  
304 Pacific and Greenland: Implications for atmospheric transport to  
305 Greenland and for the application of dust as a chronostraphic tool.  
306 *Paleoceanography* **30**, 583–600 (2015).
- 307 28. Max, L. *et al.* Pulses of enhanced North Pacific Intermediate Water  
308 ventilation from the Okhotsk Sea and Bering Sea during the last  
309 deglaciation. *Clim. Past* **10**, 591–605 (2014).
- 310 29. Keigwin, L. Glacial Age Hydrography of the Far Northwest Pacific  
311 Ocean. *Paleoceanography* **13**, 323–339 (1998).
- 312 30. Okazaki, Y. *et al.* Deepwater Formation in the North Pacific During the  
313 Last Glacial Termination. *Science* **329**, 200–204 (2010).
- 314 31. Braconnot, P. *et al.* Evaluation of climate models using palaeoclimatic  
315 data. *Nature Clim. Change* **2**, 417–424 (2012).
- 316 32. Talley, L. D. Distribution and formation of North Pacific intermediate  
317 water. *J. Phys. Oceanogr.* **23**, 517–537 (1993).
- 318 33. Max, L. *et al.* Evidence for enhanced convection of North Pacific  
319 Intermediate Water to the low-latitude Pacific under glacial conditions.  
320 *Paleoceanography* **32**, 41–55 (2017).
- 321 34. Matsumoto, K., Oba, T. & Lynch-Stieglitz, J. Interior hydrography and  
322 circulation of the glacial Pacific Ocean. *Quaternary Science Reviews*  
323 **21**, 1693–1704 (2002).

- 324 35. Rae, J. W. B. *et al.* Deep water formation in the North Pacific and  
325 deglacial CO<sub>2</sub> rise. *Paleoceanography* **29**, 645–667 (2014).
- 326 36. Cook, M. S. & Keigwin, L. Radiocarbon profiles of the NW Pacific from  
327 the LGM and deglaciation: Evaluating ventilation metrics and the effect  
328 of uncertain surface reservoir ages. *Paleoceanography* **30**, 174–195  
329 (2015).
- 330 37. Ullman, D. J., Carlson, A. E., Anslow, F. S., LeGrande, A. N. & Licciardi,  
331 J. M. Laurentide ice-sheet instability during the last deglaciation. *Nature*  
332 *Geoscience* **8**, 534–537 (2015).
- 333 38. Deutsch, C., Sigman, D. M., Thunell, R. C., Meckler, A. N. & Haug, G.  
334 H. Isotopic constraints on glacial/interglacial changes in the oceanic  
335 nitrogen budget. *Global Biogeochem. Cycles* **18**, GB4012 (2004).
- 336 39. Anderson, R. F. *et al.* Wind-Driven Upwelling in the Southern Ocean  
337 and the Deglacial Rise in Atmospheric CO<sub>2</sub>. *Science* **323**, 1443–1448  
338 (2009).
- 339 40. Burke, A. & Robinson, L. F. The Southern Ocean's Role in Carbon  
340 Exchange During the Last Deglaciation. *Science* **335**, 557–561 (2012).
- 341 41. McManus, J. F., Francois, R., Gherardi, J. M. & Keigwin, L. Collapse  
342 and rapid resumption of Atlantic meridional circulation linked to  
343 deglacial climate changes. *Nature* **428**, 834–837 (2004).
- 344 42. Knudson, K. P. & Ravelo, A. C. North Pacific Intermediate Water  
345 circulation enhanced by the closure of the Bering Strait.  
346 *Paleoceanography* **30**, PA002840 (2015).
- 347 43. Méheust, M., Stein, R., Fahl, K., Max, L. & Riethdorf, J.-R. High-  
348 resolution IP25-based reconstruction of sea-ice variability in the western

349 North Pacific and Bering Sea during the past 18,000 years. *Geo-Mar*  
350 *Lett* **36**, 101–111 (2015).

351

352 Corresponding Author: WRG; wrg4@st-andrews.ac.uk

353

### 354 **Acknowledgments**

355 We thank Michael Sarnthein for providing core material and stimulating  
356 discussions, the 'B-team' for their accommodation in the National  
357 Oceanography Centre Southampton's laboratories, Anabel Mortes Rodenas  
358 for assistance with ICP-MS analysis at Cardiff University, and Jonathan  
359 Holmes for support throughout the project. We acknowledge the World  
360 Climate Research Programme's Working Group on Coupled Modelling for the  
361 coordination of CMIP and thank the climate modeling groups for producing  
362 and making available their model output ([https://esgf-](https://esgf-node.llnl.gov/search/cmip5/)  
363 [node.llnl.gov/search/cmip5/](https://esgf-node.llnl.gov/search/cmip5/)). We thank three anonymous reviewers for their  
364 thoughtful comments and detailed suggestions that substantially improved this  
365 paper. This work was funded by NERC studentship NE/I528185/1 awarded to  
366 W.R.G., NERC studentship NE/1492942/1 to B.T., NERC grant  
367 NE/N011716/1 awarded to J.W.B.R and A.B., and NERC grant NE/I013377/1  
368 awarded to A.E.S.

369

### 370 **Author contributions**

371 W.R.G. and J.W.B.R. designed the study and wrote the manuscript; W.R.G.,  
372 J.W.B.R, G.L.F., C.H.L., and A.E.S. were involved in the generation of the  
373 trace element and  $\delta^{11}\text{B}$  data; R.C.W. analysed climate model output; all



374 authors contributed to the interpretation and preparation of the final  
375 manuscript.

376

### 377 **Financial competing interests**

378 The authors declare no competing financial interests.

379

### 380 *Figure captions*

381

382 **Figure 1. CO<sub>2</sub> and nutrients in the modern subpolar North Pacific (a)**  
383 annual surface ocean-atmosphere CO<sub>2</sub> flux<sup>17</sup>, with contours of surface ocean  
384 phosphate (PO<sub>4</sub>) in μmol/kg<sup>18</sup>. The location of core MD01-2416 (51.27°N,  
385 167.73°E, 2317 m water depth) is indicated by a star **(b)** upper water column  
386 profiles of dissolved inorganic carbon (DIC) and phosphate in the western  
387 subpolar North Pacific<sup>15</sup>.

388

389 **Figure 2. Deglacial changes in the biogeochemistry of the subpolar**  
390 **North Pacific (a)** δ<sup>11</sup>B of *N. pachyderma* from MD01-2416 **(b)** pH with LOESS  
391 smooth and 1σ and 2σ error envelope (Methods). The star shows pre-  
392 industrial pH at this site<sup>20</sup> (50m water depth) and blue lines show equilibrium  
393 pH (Methods) **(c)** Opal MAR from MD01-2416<sup>21</sup> (filled circles, inset-axis),  
394 RAMA-PC-44<sup>9</sup> (triangles), PC13<sup>22</sup> (squares), ODP882<sup>23</sup> (open circles) and  
395 SO202-07-6<sup>19</sup> (inverse triangles) **(d)** Excess U (dark pink) and Mo (light pink)  
396 from EW0408-85JC<sup>11,24</sup> **(e)** δ<sup>15</sup>N of *N. pachyderma* from SO202-07-6<sup>19</sup>  
397 (diamonds), diatoms from PC13<sup>22</sup> (squares), and bulk sediments from MD01-  
398 2416<sup>25</sup> (dashed line), ODP887<sup>25</sup> (solid line) and ODP1017<sup>26</sup> (dotted line) **(f)**

399  $^4\text{He}$  flux from SO202-7-6<sup>27</sup>. YD, B/A and HS1 are the Younger Dryas, Bølling  
400 Allerød, and Heinrich Stadial 1. See supplement for core locations.

401

402 **Figure 3. Deglacial temperature,  $p\text{CO}_2$  and NPIW formation (a) *N.***  
403 *pachyderma* Mg/Ca-temperature with LOESS smooth and  $1\sigma$  and  $2\sigma$  error  
404 envelope. The star shows modern mean annual temperature at the site<sup>18</sup>  
405 (50m water depth) **(b)  $p\text{CO}_2$**  in the atmosphere<sup>4</sup> and near-surface subpolar  
406 North Pacific with LOESS smooth and  $1\sigma$  and  $2\sigma$  error envelope (Methods).  
407 The star shows pre-industrial  $p\text{CO}_2$  at the site<sup>20</sup> (50m water depth) **(c)  $\delta^{13}\text{C}$**  of  
408 *Cibicidoides* spp. from the intermediate Bering Sea (SO201-2-85KL) and  
409 Okhotsk Sea (SO178-13-6)<sup>28</sup> (Methods). The triangle shows the LGM value  
410 for the intermediate-depth (~1000 m) Okhotsk Sea<sup>29</sup> **(d) Benthic-planktic  $^{14}\text{C}$**   
411 age difference in the intermediate depth (<1500 m) northwest Pacific<sup>30</sup> with  $1\sigma$   
412 error bars and LOESS smooth; CH84-14 (circles), GH02-1030 (triangles), and  
413 MR01K03-PC4/PC5 (diamonds). The star shows pre-bomb benthic-planktic  
414  $^{14}\text{C}$  age<sup>20</sup>.

415

416 **Figure 4. Wind stress curl in the glacial North Pacific. (a) PMIP3**  
417 ensemble mean difference in wind stress curl in the North Pacific in LGM  
418 relative to the pre-industrial (PI) control (positive means greater wind stress  
419 curl in LGM), with changes in vector windstress indicated by the arrows (see  
420 grey arrow in top left corner for scale) **(b) PI and LGM windstress curl**  
421 between  $40^\circ\text{N}$  and  $60^\circ\text{N}$  (shown by the black box in a, corresponding to the  
422 position of the subpolar gyre under PI conditions) in each of the models. The  
423 ensemble means for the PI and LGM are shown by the stars.

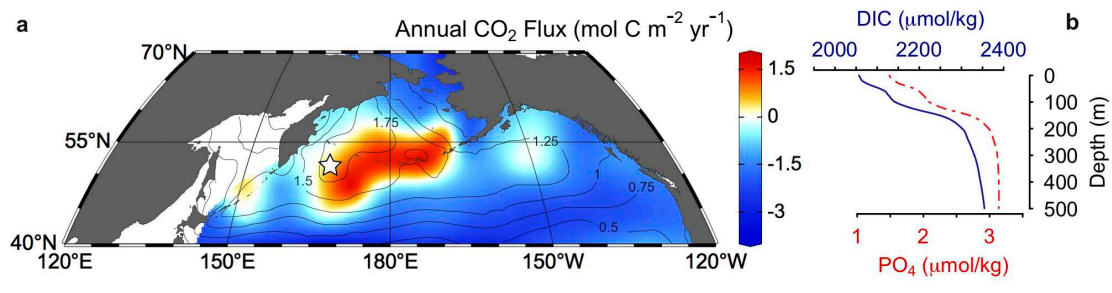


Figure 1

424

425

426

427

428

429

430

431

432

433

434

435

436

437

438

439

440

441

442

443

444

445

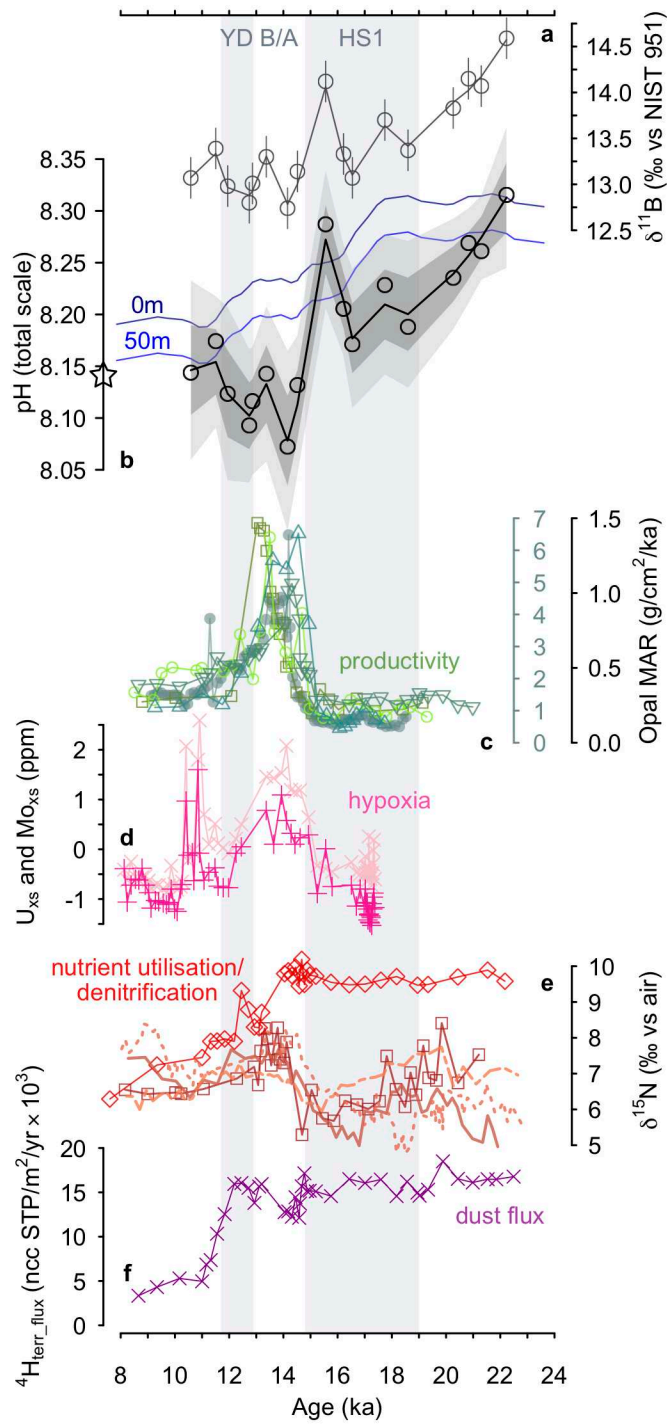


Figure 2

446

447

448

449

450

451

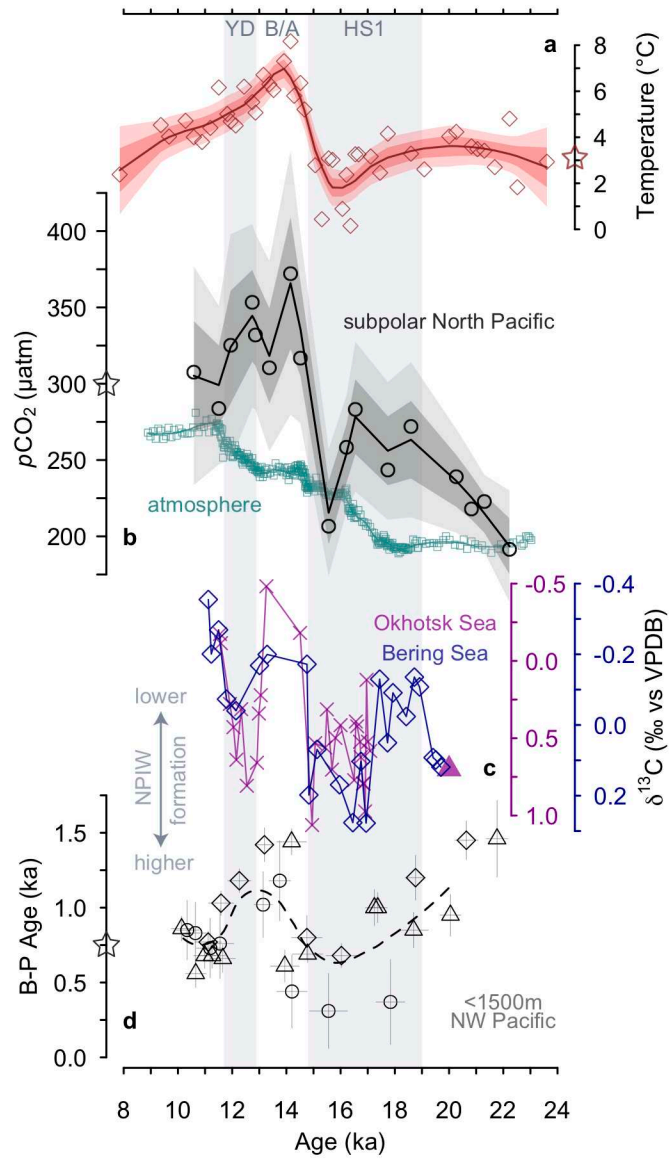


Figure 3

452

453

454

455

456

457

458

459

460

461

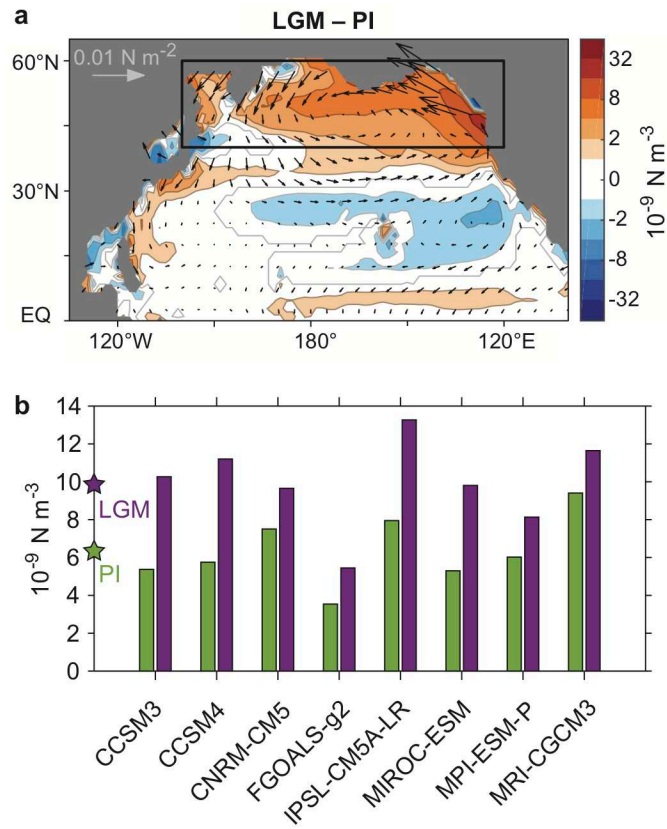


Figure 4

462

463

464

465

466

467

468

469

470

471

472

473

474

475

476

477 **Methods**

478 *Data availability*

479 The authors declare that data supporting the findings of this study are  
480 available within the article and its supplementary information files. Data are  
481 also available on *Pangaea* (doi.pangaea.de/10.1594/PANGAEA.887381).

482

483 *Habitat depth and seasonality of *N. pachyderma* in the western North Pacific*

484 Sediment trap data in the modern NW Pacific display two seasonal *N.*  
485 *pachyderma* abundance peaks during the spring and autumn, roughly  
486 corresponding to the time of most, and least, stratification respectively. As  
487 these fluxes are more or less equal, the geochemical signature of *N.*  
488 *pachyderma* should represent mean annual oceanographic conditions at a  
489 water depth of ~50 m<sup>44</sup>, provided that the growing season of *N. pachyderma*  
490 did not change substantially in the past.

491

492 *Core materials*

493 Core MD01-2416 was raised from 51.27°N, 167.73°E, 2317 m water depth on  
494 the Detroit Seamount. This site is situated within the subpolar North Pacific  
495 High Nutrient Low Chlorophyll zone, making it well suited to track past  
496 changes in CO<sub>2</sub> outgassing in this region (Figure 1). %Opal data from the  
497 core (Figure 2) were previously published (refs<sup>21,45</sup>), and were converted into  
498 mass accumulation rate (MAR) using the age model described below.  
499 Foraminifera are well-preserved throughout the deglaciation in this core, likely  
500 due to its high sedimentation rate and the relatively muted changes in  
501 carbonate ion since the LGM in the deep Pacific<sup>46</sup>.

502

503 *Age model for MD01-2416*

504 We generated a new age model for the core by recalibrating 36 *N.*  
505 *pachyderma* <sup>14</sup>C dates from ref<sup>47</sup>, excluding 6 <sup>14</sup>C dates previously  
506 demonstrated to show evidence of reworking<sup>47</sup>. The <sup>14</sup>C dates were calibrated  
507 with INTCAL13<sup>48</sup>. There are likely to be considerable changes in deglacial  
508 reservoir age which are difficult to constrain; we apply a constant reservoir  
509 age of 950±450 yrs, which encompasses the modern seasonal variability  
510 within the region, as well as paleo-reconstructions and model estimates for  
511 the LGM, deglaciation, and the Holocene<sup>20,49-52</sup>. The age model was  
512 constructed using the BACON<sup>53</sup> Bayesian age modelling package in R.  
513 Uncertainty in calibrated age is typically ±800 years at the 95% confidence  
514 interval, increasing to greater than ±1000 years before ~21ka. Using the <sup>14</sup>C  
515 plateau tuned chronology of ref<sup>47</sup> makes no difference to any of the  
516 conclusions drawn (Supplementary Figure 4).

517

518 *δ<sup>11</sup>B and trace element analysis*

519 Well-preserved *N. pachyderma* were picked from the 150-250 μm size fraction  
520 at a 3-15 cm resolution. ~400 individuals were used per δ<sup>11</sup>B analysis.  
521 Samples were cleaned in a class 100 clean lab at the National Oceanography  
522 Centre Southampton (NOCS) according to the 'Mg' method of ref<sup>54</sup> as detailed  
523 in ref<sup>55</sup>. A ~5% split of the cleaned foraminiferal samples was analysed after  
524 acidification for a suite of trace elements at NOCS using an Element II HR-  
525 ICP-MS against matrix matched standards. δ<sup>11</sup>B was analysed at NOCS on a  
526 Neptune MC-ICP-MS following the method of ref<sup>55,56</sup>, which involves removing



527 the sample matrix prior to analysis using anionic exchange resin, and sample-  
528 standard bracketing to correct for instrument induced mass fractionation. Long  
529 term reproducibility of this approach is  $\pm 0.23\%$  at the 95% confidence  
530 interval<sup>57</sup>.

531

532 To increase the resolution of the Mg/Ca record, 26 additional samples were  
533 analysed for trace elements only. Between 20-50 individual *N. pachyderma*  
534 were cleaned following the oxidative/reductive protocol of ref<sup>58</sup>. The samples  
535 were analysed at Cardiff University using an Element II HR-ICP-MS against  
536 matrix-matched standards. The same standards were used at both Cardiff  
537 University and NOCS to ensure consistency.

538

539 Average Al/Ca values are  $\sim 50$   $\mu\text{mol/mol}$ . Six samples have Al/Ca between  
540 100-150  $\mu\text{mol/mol}$ , however these samples do not display elevated Mg/Ca or  
541 B/Ca indicating no influence of clay contamination. Average Mn/Ca for  
542 samples cleaned using the 'Mg' method is 80  $\mu\text{mol/mol}$ , whereas average  
543 Mn/Ca for reductively cleaned samples is  $<10$   $\mu\text{mol/mol}$ . Despite the higher  
544 Mn/Ca values of the 'Mg' cleaned samples, both datasets display very similar  
545 Mg/Ca (after correction for preferential dissolution of high-Mg calcite during  
546 reductive cleaning<sup>54</sup>) and B/Ca values downcore, indicating no influence of  
547 Mn-Fe oxyhydroxide coatings. Previously published Mg/Ca data from MD01-  
548 2416<sup>21,45</sup> show elevated values compared to the data cleaned by both the 'Mg'  
549 method and the reductive method in this study, indicating a possible influence  
550 of contamination, so are not used in our temperature reconstruction. Including  
551 these data makes no difference to any of the conclusions drawn.

552

553 *Temperature record*

554 The Mg/Ca values were converted to temperature using the species specific  
555 calibration of ref<sup>59</sup> (recalculated by ref<sup>60</sup>). Samples that had been reductively  
556 cleaned were adjusted upward by 12.5% to account for preferential  
557 dissolution of high-Mg calcite during reductive cleaning<sup>54</sup>. The data were fitted  
558 with a non-parametric regression (LOESS) in R. The smoothing parameter ( $\alpha$ )  
559 was optimised using generalised cross validation (GCV). A Monte Carlo  
560 approach was used to determine the most likely fit to the data, with the  
561 LOESS smooth fitted to ten thousand realisations of the temperature data with  
562 an uncertainty of  $\pm 2.3$  °C ( $2\sigma$ ), accounting for the 1.2 °C ( $2\sigma$ ) calibration  
563 error<sup>59</sup>, and incorporating terms for uncertainty in salinity ( $\pm 2$  PSU [ $2\sigma$ ] with a  
564 sensitivity of 3%/PSU<sup>61,62</sup>), and pH ( $\pm 0.2$  pH units [ $2\sigma$ ] with a sensitivity of -  
565 7%/0.1 pH units<sup>62,63</sup>).

566

567 pH is known to affect planktic foraminiferal Mg/Ca with a sensitivity of ~-  
568 7%/0.1 pH units<sup>62,63</sup>. While the pH minimum during the Bølling-Allerød may be  
569 influencing the apparent Mg/Ca temperatures, this influence is likely to be  
570 minimal. Firstly, as the absolute value of pH during the Bølling-Allerød  
571 interval is broadly equivalent to pre-industrial (it is a large anomaly from  
572 equilibrium due to lower atmospheric CO<sub>2</sub> concentrations during the Bølling-  
573 Allerød) the effect of pH on absolute temperature will be negligible. Secondly,  
574 the  $\Delta$ pH at the onset of the Bølling-Allerød is ~0.15 units, so given a Mg/Ca  
575 sensitivity of -7%/0.1 pH units, this could only account for a 10% increase in  
576 Mg/Ca, or ~1-1.5 °C, considerably smaller than the ~5 °C warming indicated

577 by the Mg/Ca record at the onset of the Bølling-Allerød. The effect of higher  
578 pH during the LGM means our Mg/Ca temperature record is likely to be  
579 underestimating LGM temperature by ~1-1.5 °C. Dissolution can also effect  
580 foraminiferal Mg/Ca, though this influence is relatively minor in lower-Mg  
581 planktic foraminifera such as *N. pachyderma*<sup>64</sup>. LGM-Holocene changes in  
582 bottom water carbonate ion concentration are also relatively minor within the  
583 Pacific (~10 µmol/kg)<sup>46</sup>, and our Mg/Ca data show no correlation with  
584 %CaCO<sub>3</sub> in this core, so dissolution is unlikely to have a significant influence  
585 on our record. Our temperature record shows good agreement with the  
586 assemblage derived temperature record of ref<sup>21,45</sup> from the same core. Recent  
587 research found that the *G. ruber* Mg/Ca-temperature sensitivity is lower than  
588 the widely applied 9%/°C temperature sensitivity<sup>62</sup>; if future calibration work  
589 also demonstrates similar results for *N. pachyderma*, our Mg/Ca-temperature  
590 record may need minor revision.

591

### 592 *Carbonate system calculations*

593 To calculate pH the  $\delta^{11}\text{B}$  of *N. pachyderma* was converted to seawater  
594  $\delta^{11}\text{B}_{\text{borate}}$  using the calibration of ref<sup>65</sup>, where  $\delta^{11}\text{B}_{\text{borate}} = \delta^{11}\text{B}_{\text{Npachyderma}} +$   
595  $3.38 \pm 0.71\text{‰}$  ( $2\sigma$ ). To fully explore the uncertainty associated with the  
596 calibration, we recalibrated the dataset of ref<sup>65</sup>, varying the slope between 0.6  
597 and 1.4 (which incorporates the range previously observed in all other species  
598 of planktic foraminifera, refs<sup>16,66,67</sup>) with a flat probability distribution, allowing  
599 the intercept to vary (see sensitivity test below). pH was calculated from  
600  $\delta^{11}\text{B}_{\text{borate}}$  using a seawater  $\delta^{11}\text{B}$  value of 39.61‰<sup>68</sup> and the experimentally-  
601 determined fractionation factor of 1.0272<sup>69</sup> following ref<sup>70</sup>. The boric acid

602 dissociation constant ( $K_B$ ) was calculated with the Mg/Ca temperature, and an  
603 estimate of salinity generated by taking the salinity at the site today (33.0  
604 PSU), and accounting for the whole ocean change in salinity over deglaciation  
605 by scaling the 1.15 PSU glacial salinity increase of ref<sup>71</sup> to the sea level curve  
606 of ref<sup>72</sup>. To fully propagate uncertainty in reconstructed pH a Monte-Carlo  
607 approach was taken, with ten thousand realisations of the data accounting for  
608 the uncertainties in the measurement of  $\delta^{11}\text{B}_{\text{Npachyderma}}$ , the conversion of the  
609  $\delta^{11}\text{B}_{\text{Npachyderma}}$  to  $\delta^{11}\text{B}_{\text{borate}}$ , and of the uncertainty in the temperature and  
610 salinity reconstructions on  $K_B$  using the confidence interval of the LOESS  
611 temperature smooth and a salinity uncertainty of  $\pm 2$  units ( $2\sigma$ ). Typical  
612 uncertainty on the pH reconstruction following this approach is  $\pm 0.084$  ( $2\sigma$ ),  
613 which is chiefly due to the uncertainty in the offset between the  $\delta^{11}\text{B}$  of *N.*  
614 *pachyderma* and seawater  $\delta^{11}\text{B}_{\text{borate}}$  ( $\pm 0.078$   $2\sigma$ ). Using a constant value of  $K_B$   
615 (i.e. constant temperature and salinity) has no major influence on  
616 reconstructed pH values (see sensitivity test). Preservation has not been  
617 shown to influence planktic  $\delta^{11}\text{B}$ <sup>73</sup>.

618

619 An additional parameter of the carbonate system is required to calculate  $p\text{CO}_2$   
620 from pH, and total alkalinity is widely used<sup>16,56,65</sup>. Although modeling studies  
621 can provide estimates of the change in alkalinity during the LGM<sup>1,74</sup>, there are  
622 few data-based constraints on its secular evolution over deglaciation. Here we  
623 follow the approach of ref<sup>16</sup>, taking a range in alkalinity between modern day  
624 alkalinity at the site ( $2235 \mu\text{mol/kg}$ )<sup>20</sup> plus an estimate of the glacial alkalinity  
625 increase based on the modeling results of refs<sup>1,74</sup> ( $+125 \mu\text{mol/kg}$ ), and  
626 modern day alkalinity at the site minus  $25 \mu\text{mol/kg}$ , with a 'flat' probability

627 distribution between these values. With this approach there is an equal  
628 probability of total alkalinity being at any value between 2210 and 2360  
629  $\mu\text{mol/kg}$  at any point in the record, fully exploring the likely range in alkalinity  
630 without giving weight to any particular value. Note, this range in alkalinity is  
631 cautious, being broadly equivalent to the range observed across the surface  
632 of the entire open Pacific Ocean today<sup>20</sup>. The  $p\text{CO}_2$  of seawater was  
633 calculated using the *seacarb* package in R<sup>75</sup>, using the constants of refs<sup>76-78</sup>.  
634 To fully propagate the uncertainty associated with each parameter ten  
635 thousand realisations of pH, total alkalinity, temperature and salinity were  
636 input, using the uncertainty on each parameter described above. Following  
637 this approach, the total uncertainty associated with our  $p\text{CO}_2$  estimates is  
638 typically  $\pm 64 \mu\text{atm}$  ( $2\sigma$ ), which again is chiefly due to the uncertainty in the  
639 offset between  $\delta^{11}\text{B}_{\text{Npachyderma}}$  and  $\delta^{11}\text{B}_{\text{borate}}$  ( $\pm 55 \mu\text{atm}$ ).  $p\text{CO}_2$  estimates are  
640 almost entirely driven by the pH estimates (Supplementary Figure 5). Typical  
641  $p\text{CO}_2$  uncertainty associated with the temperature uncertainty is  $\pm 2 \mu\text{atm}$  ( $2\sigma$ ),  
642 and the uncertainty associated with the salinity uncertainty is  $\pm 10 \mu\text{atm}$  ( $2\sigma$ ).  
643 Using either a constant 'modern minus 25  $\mu\text{mol/kg}$ ' or 'modern plus 125  
644  $\mu\text{mol/kg}$ ' total alkalinity changes the  $p\text{CO}_2$  values by only  $\pm 20 \mu\text{atm}$ .

645

646 Surface ocean pH at equilibrium with the atmosphere was calculated using  
647 alkalinity calculated in the manner described above, and the atmospheric  $\text{CO}_2$   
648 record of ref<sup>4</sup>. Salinity (estimated in the manner described above) and Mg/Ca  
649 temperature were used to constrain changes in dissociation constants.  
650 Equilibrium pH at 50m is calculated by applying the modern surface-50m pH  
651 gradient ( $-0.035$  units); deviations from equilibrium pH therefore represent

652 changes in the carbonate system beyond those expected from changing  
653 atmospheric CO<sub>2</sub>.

654

655 Both the pH and pCO<sub>2</sub> records were fitted with a LOESS smooth in R, with the  
656 smoothing parameter ( $\alpha$ ) determined by GCV. To determine the most likely fit  
657 to the data a LOESS smooth fitted to ten thousand realisations of the data,  
658 accounting for the uncertainties in the pH and pCO<sub>2</sub> estimates in the manner  
659 described above; this approach allows us to identify significant trends within  
660 the data and reduce uncertainty in our estimates.

661

#### 662 *Carbonate system sensitivity tests*

663 As the current  $\delta^{11}\text{B}_{\text{calcite}}-\delta^{11}\text{B}_{\text{borate}}$  calibration for *N. pachyderma* comes from a  
664 limited range in pH<sup>65</sup>, application of this calibration to the NW Pacific requires  
665 extrapolation beyond the calibrated range. We tested the sensitivity of our  
666 results to the assumed slope of calibration, building on the test outlined in  
667 ref<sup>79</sup>. We re-calibrated the coretop data of ref<sup>65</sup>, forcing the slope within the  
668 range previously observed in all other species of planktic foraminifera  
669 (refs<sup>16,66,67</sup>), while allowing the intercept to vary (Supplementary Figure 6).  
670 This exercise demonstrates that within the range previously observed in all  
671 other species of planktic foraminifera, the assumed slope of the  $\delta^{11}\text{B}_{\text{calcite}}-$   
672  $\delta^{11}\text{B}_{\text{borate}}$  calibration makes no difference to any of the conclusions drawn in  
673 this study.

674

675 To provide a further constraint on the relationship between  $\delta^{11}\text{B}_{\text{Npachyderma}}$  and  
676  $\delta^{11}\text{B}_{\text{borate}}$ , we measured the  $\delta^{11}\text{B}$  of *N. pachyderma* (following the method

677 described above) from Holocene sediments in core MD02-2489 (54.39°N,  
678 148.92°E, 3640 m water depth), located in the eastern subpolar Pacific, where  
679 modern pH values are significantly higher than in the western subpolar  
680 Pacific. Comparing this data along with the Holocene  $\delta^{11}\text{B}_{\text{Npachyderma}}$  data from  
681 site MD01-2416 to pre-industrial  $\delta^{11}\text{B}_{\text{borate}}$  (calculated from ref<sup>20</sup>) shows  
682 excellent agreement with the *N. pachyderma*  $\delta^{11}\text{B}_{\text{calcite}}-\delta^{11}\text{B}_{\text{borate}}$  calibration  
683 proposed by ref<sup>65</sup> over a range of  $\delta^{11}\text{B}$  ~equivalent to our down-core  
684 reconstruction (Supplementary Figure 6).

685

686 To test the sensitivity of our pH and  $p\text{CO}_2$  reconstructions to temperature, we  
687 calculated pH and  $p\text{CO}_2$  assuming constant temperatures of 2 °C, 5 °C and 8  
688 °C (broadly the deglacial range suggested by the Mg/Ca). Supplementary  
689 Figure 7 demonstrates that using a constant temperature in our carbonate  
690 system calculations would not have any effect on the main findings of this  
691 study. Compiling all available proxy temperature data in the western subpolar  
692 North Pacific demonstrates that using the reconstructed temperatures  
693 suggested by all available proxies (Mg/Ca,  $\text{U}^{\text{k}}_{37}$ , TEX<sub>86</sub>, foraminiferal  
694 assemblage transfer function; refs<sup>21,80-82</sup>) in our carbonate system calculations  
695 results in a substantial outgassing of  $\text{CO}_2$  from the subpolar North Pacific  
696 during the Bølling-Allerød.

697

#### 698 *Overtuning and $\text{CO}_2$ in early deglaciation*

699 In addition to the large decrease in pH at the onset of the Bølling-Allerød, our  
700 record demonstrates a decrease in pH during early deglaciation, reaching a  
701 minimum in HS1. Benthic foraminiferal  $\delta^{13}\text{C}$  and radiocarbon records show an

702 increase in overturning circulation during early deglaciation relative to the  
703 LGM<sup>28,30</sup>, with possible local deepwater formation during HS1<sup>30,35</sup>  
704 (Supplementary Figure 8). The deepening of the overturning circulation during  
705 early-deglaciation would have allowed deeply sequestered nutrients and CO<sub>2</sub>  
706 to mix more vigorously through the water column<sup>35</sup>, resulting in the observed  
707 decrease in pH and increase in CO<sub>2</sub> in the near-surface ocean, and  
708 outgassing of CO<sub>2</sub> to the atmosphere. The increase in overturning would have  
709 resulted in a deepening of the mixed layer, such that light may have become  
710 limiting to primary production<sup>14</sup>. A return to a shallower overturning circulation  
711 (similar to the LGM) during late-HS1 would have lessened the upward mixing  
712 of deep carbon, increasing pH. Note, removing the high-pH data point at  
713 ~15.5 ka makes no difference to any of the conclusions drawn in this study;  
714 even without this high-pH data point there is a ~0.1 pH unit decrease from the  
715 mean HS1 value going into the B/A, indicating a substantial increase in  
716 nutrient- and CO<sub>2</sub>- supply.

717

#### 718 *Nutrient utilisation/denitrification controls on $\delta^{15}N$*

719 Nitrogen isotope records may be influenced by both the degree of nitrate  
720 utilisation and the isotopic composition of nitrate in the source  
721 water<sup>22,25,38,83,84</sup>. The widespread hypoxia accompanying the Bølling-Allerød  
722 productivity maximum is thought to have significantly increased denitrification  
723 within the oxygen minimum zones of the northeast Pacific<sup>22,26,83,84</sup>, driving up  
724 the  $\delta^{15}N$  of seawater nitrate. This is reflected by the large increase in bulk  
725 sediment  $\delta^{15}N$  in cores from the Mexican<sup>83</sup> and Californian<sup>26</sup> continental  
726 margins to the Alaskan gyre<sup>25</sup> (Figure 2). This signal is spread throughout the



727 subsurface North Pacific<sup>25</sup>, influencing the  $\delta^{15}\text{N}$  of nitrate upwelled in the  
728 northwest Pacific. Records of  $\delta^{15}\text{N}$  from the northwest Pacific (including bulk-  
729 sediment, diatom-bound, and foram-bound  $\delta^{15}\text{N}$ ) show relatively muted  
730 changes at the onset of the Bølling-Allerød<sup>19,22,25</sup>. This likely reflects the  
731 opposing influences of a decrease in nutrient utilisation, due to higher nutrient  
732 supply in this key upwelling region, and the increase in  $\delta^{15}\text{N}$  of source water  
733 nitrate due to hypoxia-driven denitrification.

734

#### 735 *Constraints on CO<sub>2</sub> uptake within the mixed layer*

736 CO<sub>2</sub> concentrations in the mixed layer are likely to be lower than at the ~50m  
737 depth habitat of *N. pachyderma*. However, the mean annual difference  
738 between 50 m and surface ocean at this core site today is only ~10  $\mu\text{atm}$ .  
739 During the summer months this difference is 21.9  $\mu\text{atm}$ <sup>20</sup>, due export  
740 production from the mixed layer, and during winter is close to zero due to  
741 mixing of the upper water column. While it is possible this difference was  
742 higher in the past, the Mg/Ca of the *N. pachyderma* indicates temperatures of  
743 5-7 °C during the interval of low pH/high CO<sub>2</sub> suggesting that either (a) the *N.*  
744 *pachyderma* are recording a signal close to the surface at this time, (b) the  
745 mixed layer was deeper and thus thermal stratification weak, or (c) the *N.*  
746 *pachyderma* are recording a summer signal at this time, which would make  
747 the CO<sub>2</sub> concentrations a minimum estimate. All of these scenarios would  
748 result in a significant flux of CO<sub>2</sub> to the atmosphere.

749

#### 750 *CO<sub>2</sub> outgassing and atmospheric CO<sub>2</sub> change*

751 Net changes in atmospheric CO<sub>2</sub> on millennial timescales are strongly  
752 influenced by the inventory of preformed versus remineralised nutrients in the  
753 ocean's interior<sup>74,85</sup>. Constraining preformed nutrient inventory is challenging  
754 using paleo-proxies. However, given the increased nutrient consumption<sup>19</sup>  
755 and high pH/low CO<sub>2</sub> of the near-surface North Pacific during the LGM  
756 (Figures 1 and 2), Glacial NPIW would likely have had lower preformed  
757 nutrient content than the water in the upper 1500m of the North Pacific  
758 today<sup>86</sup>. Overall this would make the biological pump more efficient at the  
759 LGM, driving down atmospheric CO<sub>2</sub>. At the onset of the Bølling-Allerød, our  
760 data suggest a net weakening in the strength of the North Pacific biological  
761 pump and substantial outgassing of CO<sub>2</sub> from near surface waters. The  
762 collapse in NPIW formation at this time would also have removed this source  
763 of relatively low-preformed nutrient water from the ocean's interior, and thus  
764 would also act to increase atmospheric CO<sub>2</sub>.

765

#### 766 *Benthic $\delta^{13}\text{C}$ records*

767 The benthic  $\delta^{13}\text{C}$  records (*Cibicidoides* spp.) were corrected for the whole  
768 ocean change in  $\delta^{13}\text{C}$  relating to changes in the terrestrial biosphere by  
769 scaling the value of ref<sup>87</sup> to global sea level<sup>72</sup>. This only affects the long-term  
770 trend, and makes no difference to millennial scale events within the records.

771

#### 772 *PMIP3 model output*

773 We analyse the difference in North Pacific wind-stress curl between LGM and  
774 Preindustrial (PI) conditions as represented by 8 coupled climate models  
775 (listed in Figure 4b). All models but CCSM3 are part of the Coupled Model

776 Intercomparison Project phase 5 (CMIP5). Orbital parameters, atmospheric  
777 greenhouse gas concentrations, coastlines, and ice topography for the LGM  
778 simulations are standardized as part of the Paleoclimate Model  
779 Intercomparison Project phase 3 (PMIP3) and represent best estimates of the  
780 climate state at the LGM, 21 ka before present<sup>10</sup>. We include data from  
781 comparable LGM and PI simulations<sup>88,89</sup> using an older model, CCSM3, used  
782 extensively in paleoclimate studies. We compute the wind stress curl  
783 climatology based on the atmospheric output of each model. The computed  
784 wind stress curl is linearly interpolated onto a common grid to compute the  
785 ensemble mean (Figure 4a). Individual model results are shown on  
786 Supplementary Figure 9.

787

#### 788 **References only in Methods**

789

- 790 44. Kuroyanagi, A., Kawahata, H. & Nishi, H. Seasonal variation in the  
791 oxygen isotopic composition of different-sized planktonic foraminifer  
792 *Neogloboquadrina pachyderma* (sinistral) in the northwestern North  
793 Pacific and implications for reconstruction of the paleoenvironment.  
794 *Paleoceanography* **26**, PA4215 (2011).
- 795 45. Sarthein, M. *et al.* Mid Holocene origin of the sea-surface salinity low  
796 in the subarctic North Pacific. *Quaternary Science Reviews* **23**, 2089–  
797 2099 (2004).
- 798 46. Yu, J. *et al.* Responses of the deep ocean carbonate system to carbon  
799 reorganization during the Last Glacial-interglacial cycle. *Quaternary*  
800 *Science Reviews* **76**, 39–52 (2013).

- 801 47. Sarnthein, M., Schneider, B. & Grootes, P. M. Peak glacial <sup>14</sup>C  
802 ventilation ages suggest major draw-down of carbon into the abyssal  
803 ocean. *Clim. Past* **9**, 2595–2614 (2013).
- 804 48. Reimer, P. J. *et al.* IntCal13 and Marine13 radiocarbon age calibration  
805 curves 0-50,000 years cal BP. *Radiocarbon* **55**, 1869–1887 (2013).
- 806 49. Takahashi, T., Olafsson, J., Goddard, J. G., Chipman, D. W. &  
807 Sutherland, S. C. Seasonal variation of CO<sub>2</sub> and nutrients in the high-  
808 latitude surface oceans: A comparative study. *Global Biogeochem.*  
809 *Cycles* **7**, 843–878 (1993).
- 810 50. Butzin, M., Prange, M. & Lohmann, G. Readjustment of glacial  
811 radiocarbon chronologies by self-consistent three-dimensional ocean  
812 circulation modeling. *Earth and Planetary Science Letters* **317-318**,  
813 177–184 (2012).
- 814 51. Kovanen, D. J. & Easterbrook, D. J. Paleodeviations of radiocarbon  
815 marine reservoir values for the northeast Pacific. *Geol* **30**, 243–246  
816 (2002).
- 817 52. Southon, J. R., Nelson, D. E. & Vogel, J. S. A record of past ocean-  
818 Atmosphere radiocarbon differences from the northeast Pacific.  
819 *Paleoceanography* **5**, 197–206 (1990).
- 820 53. Blaauw, M. & Christen, J. A. Flexible paleoclimate age-depth models  
821 using an autoregressive gamma process. *Bayesian Analysis* (2011).  
822 doi:10.1214/11-BA618
- 823 54. Barker, S., Greaves, M. & Elderfield, H. A study of cleaning procedures  
824 used for foraminiferal Mg/Ca paleothermometry. *Geochem. Geophys.*

- 825 *Geosyst.* **4**, 8407 (2003).
- 826 55. Rae, J. W. B., Foster, G. L., Schmidt, D. N. & Elliott, T. Boron isotopes  
827 and B/Ca in benthic foraminifera: Proxies for the deep ocean carbonate  
828 system. *Earth and Planetary Science Letters* **302**, 403–413 (2011).
- 829 56. Foster, G. L. Seawater pH,  $p\text{CO}_2$  and  $[\text{CO}_3^{2-}]$  variations in the  
830 Caribbean Sea over the last 130 kyr: A boron isotope and B/Ca study of  
831 planktic foraminifera. *Earth and Planetary Science Letters* **271**, 254–266  
832 (2008).
- 833 57. Foster, G. L. *et al.* Interlaboratory comparison of boron isotope analyses  
834 of boric acid, seawater and marine  $\text{CaCO}_3$  by MC-ICPMS and NTIMS.  
835 *Chemical Geology* **358**, 1–14 (2013).
- 836 58. Boyle, E. A. & Keigwin, L. Comparison of Atlantic and Pacific  
837 paleochemical records for the last 215,000 years: Changes in deep  
838 ocean circulation and chemical inventories. *Earth and Planetary  
839 Science Letters* **76**, 135–150 (1985).
- 840 59. Elderfield, H. & Ganssen, G. Past temperature and  $\delta^{18}\text{O}$  of surface  
841 ocean waters inferred from foraminiferal Mg/Ca ratios. *Nature* **405**, 442–  
842 445 (2000).
- 843 60. Jonkers, L., Jiménez-Amat, P., Mortyn, P. G. & Brummer, G.-J. A.  
844 Seasonal Mg/Ca variability of *N. pachyderma* (s) and *G. bulloides*:  
845 Implications for seawater temperature reconstruction. *Earth and  
846 Planetary Science Letters* **376**, 137–144 (2013).
- 847 61. Hönisch, B. *et al.* The influence of salinity on Mg/Ca in planktic  
848 foraminifers – Evidence from cultures, core-top sediments and  
849 complementary  $\delta^{18}\text{O}$ . *Geochimica et Cosmochimica Acta* **121**, 196–213

- 850 (2013).
- 851 62. Gray, W. R. *et al.* The effects of temperature, salinity, and the carbonate  
852 system on Mg/Ca in *Globigerinoides ruber* (white): A global sediment  
853 trap calibration. *Earth and Planetary Science Letters* **482**, 607–620  
854 (2018).
- 855 63. Evans, D., Wade, B. S., Henehan, M. J., Erez, J. & Müller, W. Revisiting  
856 carbonate chemistry controls on planktic foraminifera Mg/Ca:  
857 implications for sea surface temperature and hydrology shifts over the  
858 Paleocene–Eocene Thermal Maximum and Eocene–Oligocene  
859 transition. *Clim. Past* **12**, 819–835 (2016).
- 860 64. Regenberg, M., Regenberg, A., Garbe-Schönberg, D. & Lea, D. W.  
861 Global dissolution effects on planktonic foraminiferal Mg/Ca ratios  
862 controlled by the calcite-saturation state of bottom waters.  
863 *Paleoceanography* **29**, 127–142 (2014).
- 864 65. Yu, J., Thornalley, D. J. R., Rae, J. W. B. & McCave, N. I. Calibration  
865 and application of B/Ca, Cd/Ca, and  $\delta^{11}\text{B}$  in *Neogloboquadrina*  
866 *pachyderma* (sinistral) to constrain CO<sub>2</sub> uptake in the subpolar North  
867 Atlantic during the last deglaciation. *Paleoceanography* **28**, 237–252  
868 (2013).
- 869 66. Henehan, M. J. *et al.* A new boron isotope-pH calibration for *Orbulina*  
870 *universa*, with implications for understanding and accounting for ‘vital  
871 effects’. *Earth and Planetary Science Letters* **454**, 282–292 (2016).
- 872 67. Henehan, M. J. *et al.* Calibration of the boron isotope proxy in the  
873 planktonic foraminifera *Globigerinoides ruber* for use in palaeo-CO<sub>2</sub>  
874 reconstruction. *Earth and Planetary Science Letters* **364**, 111–122

- 875 (2013).
- 876 68. Foster, G. L., Pogge von Strandmann, P. A. E. & Rae, J. W. B. Boron  
877 and magnesium isotopic composition of seawater. *Geochem. Geophys.*  
878 *Geosyst.* **11**, Q08015 (2010).
- 879 69. Klochko, K., Kaufman, A. J., Yao, W., Byrne, R. H. & Tossell, J. A.  
880 Experimental measurement of boron isotope fractionation in seawater.  
881 *Earth and Planetary Science Letters* **248**, 276–285 (2006).
- 882 70. Zeebe, R. E. & Wolf-Gladrow, D. A. *CO<sub>2</sub> in Seawater: Equilibrium,*  
883 *Kinetics, Isotopes.* (Elsevier Oceanography Series, 2001).
- 884 71. Adkins, J. F., McIntyre, K. & Schrag, D. P. The salinity, temperature,  
885 and  $\delta^{18}\text{O}$  of the glacial deep ocean. *Science* **289**, 1769–1773 (2002).
- 886 72. Lambeck, K., Rouby, H., Purcell, A., Sun, Y. & Sambridge, M. Sea level  
887 and global ice volumes from the Last Glacial Maximum to the Holocene.  
888 *Proceedings of the National Academy of Sciences* **111**, 15296–15303  
889 (2014).
- 890 73. Edgar, K. M., Anagnostou, E., Pearson, P. N. & Foster, G. L. Assessing  
891 the impact of diagenesis on  $\delta^{11}\text{B}$ ,  $\delta^{13}\text{C}$ ,  $\delta^{18}\text{O}$ , Sr/Ca and B/Ca values in  
892 fossil planktic foraminiferal calcite. *Geochimica et Cosmochimica Acta*  
893 **166**, 189–209 (2015).
- 894 74. Hain, M. P., Sigman, D. M. & Haug, G. H. Carbon dioxide effects of  
895 Antarctic stratification, North Atlantic Intermediate Water formation, and  
896 subantarctic nutrient drawdown during the last ice age: Diagnosis and  
897 synthesis in a geochemical box model. *Global Biogeochem. Cycles* **24**,  
898 GB4023 (2010).
- 899 75. Gattuso, J. P. *et al.* *Seacarb: seawater carbonate chemistry with R.* (R

- 900 Package version 3.1.2, 2017).
- 901 76. Millero, F. J., Graham, T. B., Huang, F., Bustos-Serrano, H. & Pierrot,  
902 D. Dissociation constants of carbonic acid in seawater as a function of  
903 salinity and temperature. *Marine Chemistry* **100**, 80–94 (2006).
- 904 77. Dickson, A. G. Standard potential of the reaction:  $\text{AgCl(s)} + 1/2\text{H}_2(\text{g}) =$   
905  $\text{Ag(s)} + \text{HCl(aq)}$ , and the standard acidity constant of the ion  $\text{HSO}_4^-$   
906 in synthetic sea water from 273.15 to 318.15 K. *The Journal of*  
907 *Chemical Thermodynamics* **22**, 113–127 (1990).
- 908 78. Dickson, A. G. & Riley, J. P. The estimation of acid dissociation  
909 constants in seawater media from potentiometric titrations with strong  
910 base. I. The ionic product of water -  $K_w$ . *Marine Chemistry* **7**, 89–99  
911 (1979).
- 912 79. Ezat, M. M., Rasmussen, T. L., Honisch, B., Groeneveld, J. &  
913 deMenocal, P. Episodic release of  $\text{CO}_2$  from the high-latitude North  
914 Atlantic Ocean during the last 135kyr. *Nature Communications* **8**, 1–10  
915 (2017).
- 916 80. Riethdorf, J.-R., Max, L., Nürnberg, D., Lembke-Jene, L. & Tiedemann,  
917 R. Deglacial development of (sub) sea surface temperature and salinity  
918 in the subarctic northwest Pacific: Implications for upper-ocean  
919 stratification. *Paleoceanography* **28**, 91–104 (2013).
- 920 81. Seki, O. *et al.* Reconstruction of paleoproductivity in the Sea of Okhotsk  
921 over the last 30 kyr. *Paleoceanography* **19**, PA1016 (2004).
- 922 82. Seki, O. *et al.* Large changes in seasonal sea ice distribution and  
923 productivity in the Sea of Okhotsk during the deglaciations. *Geochem.*  
924 *Geophys. Geosyst.* **10**, Q10007 (2009).



- 925 83. Ganeshram, R. S., Pedersen, T. F., Calvert, S. E., McNeill, G. W. & R,  
926 F. M. Glacial-interglacial variability in denitrification in the world's  
927 oceans: Causes and consequences. *Paleoceanography* **15**, 361–376  
928 (2000).
- 929 84. Brunelle, B. G. *et al.* Evidence from diatom-bound nitrogen isotopes for  
930 subarctic Pacific stratification during the last ice age and a link to North  
931 Pacific denitrification changes. *Paleoceanography* **22**, PA1215 (2007).
- 932 85. Ito, T. & Follows, M. J. Preformed phosphate, soft tissue pump and  
933 atmospheric CO<sub>2</sub>. *Journal of Marine Research* **63**, 813–839 (2005).
- 934 86. Talley, L. D. Closure of the global overturning circulation through the  
935 Indian, Pacific, and Southern Oceans: Schematics and transports.  
936 *oceanog* **86**, 80–97 (2013).
- 937 87. Peterson, C. D., Lisiecki, L. E. & Stern, J. V. Deglacial whole-ocean  
938  $\delta^{13}\text{C}$  change estimated from 480 benthic foraminiferal records.  
939 *Paleoceanography* **29**, 549–563 (2014).
- 940 88. Otto-Bliesner, B. L. *et al.* Climate sensitivity of moderate-and low-  
941 resolution versions of CCSM3 to preindustrial forcings. *J. Climate* **19**,  
942 2567–2583 (2006).
- 943 89. Otto-Bliesner, B. L. *et al.* Last Glacial Maximum and Holocene Climate  
944 in CCSM3. *J. Climate* **19**, 2526–2544 (2006).

945

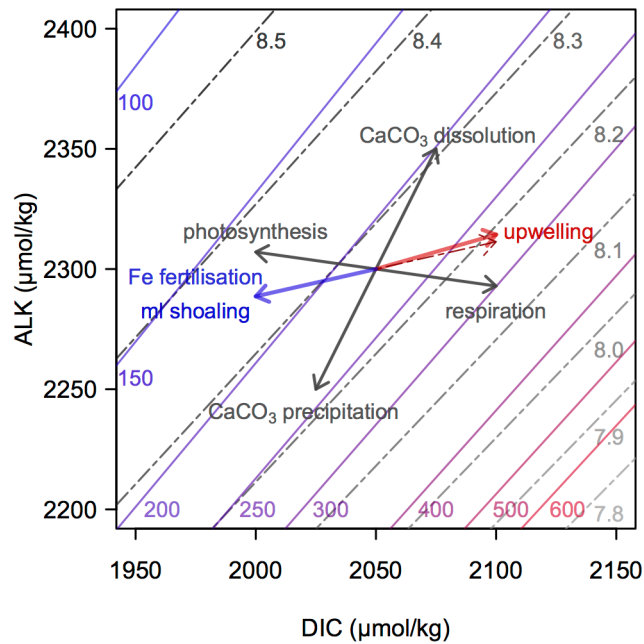
946

947

948

949

951



952

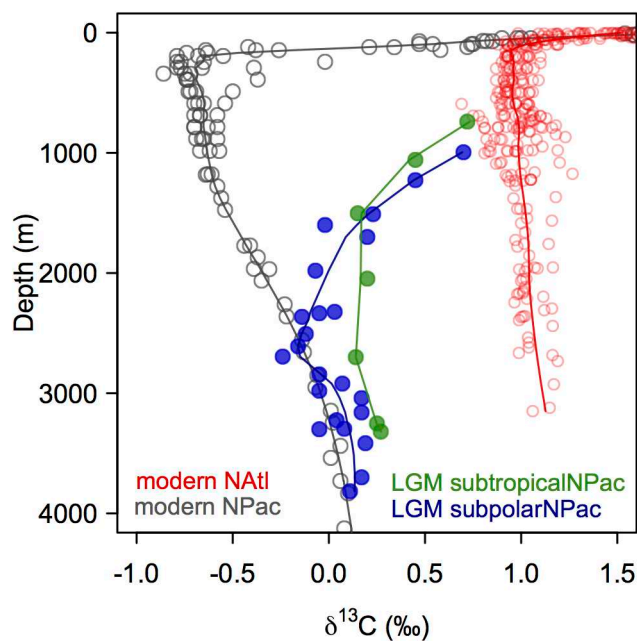
953 **Supplementary Figure 1** Dissolved Inorganic Carbon (DIC) versus Alkalinity (ALK) with  
 954 contours of pH on the total scale (grey dashed lines) and  $p\text{CO}_2$  (coloured solid lines) at 5°C,  
 955 35 PSU and 0m water depth. The effects of photosynthesis and respiration, as well as the  
 956 precipitation and dissolution of  $\text{CaCO}_3$  are indicated by the grey arrows. Formation of organic  
 957 matter by photosynthesis removes DIC and adds ALK in a ratio of ~7:1. Respiration of  
 958 organic matter adds DIC and removes ALK in the same ratio. Precipitation of  $\text{CaCO}_3$  removes  
 959 both DIC and ALK with a ratio of 1:2 and dissolution of  $\text{CaCO}_3$  adds DIC and ALK in the same  
 960 ratio. The effects of an increase in export production from iron fertilisation and mixed layer  
 961 shoaling are indicated by the blue arrow (assuming a  $C_{\text{org}}:\text{CaCO}_3$  rain ratio of 4:1). The effect  
 962 of an increase in upwelling of subsurface waters containing the respired/dissolved products  
 963 exported from a surface ocean with a  $C_{\text{org}}:\text{CaCO}_3$  rain ratio of 4:1 is shown by the solid red  
 964 arrow; the effect of upwelling waters from 250m depth into the surface of the modern western  
 965 subpolar North Pacific using the values from ref<sup>15</sup> is shown by the dashed red arrow. The  
 966 upwelling of waters from the ocean's interior brings with it the respired products of  
 967 photosynthesis, increasing the ratio of DIC to alkalinity (ALK), lowering pH and increasing  
 968  $\text{CO}_2$  (red arrow). Increasing export production through the alleviation of iron or light limitation  
 969 decreases the ratio of DIC/ALK, increasing pH and decreasing  $\text{CO}_2$  (blue arrow).

970

971

972

973



974

975 **Supplementary Figure 2**  $\delta^{13}\text{C}$  profiles of the modern (grey) and LGM (blue and green) NW  
 976 Pacific, and modern North Atlantic (red). Modern values are DIC measurements from ref<sup>15</sup>.  
 977 LGM values are *Cibicidoides* spp. from refs<sup>29,34</sup>. LGM values have been corrected for the  
 978 whole ocean change in  $\delta^{13}\text{C}$  using ref<sup>87</sup>.

979

980

981

982

983

984

985

986

987

988

989

990

991

992

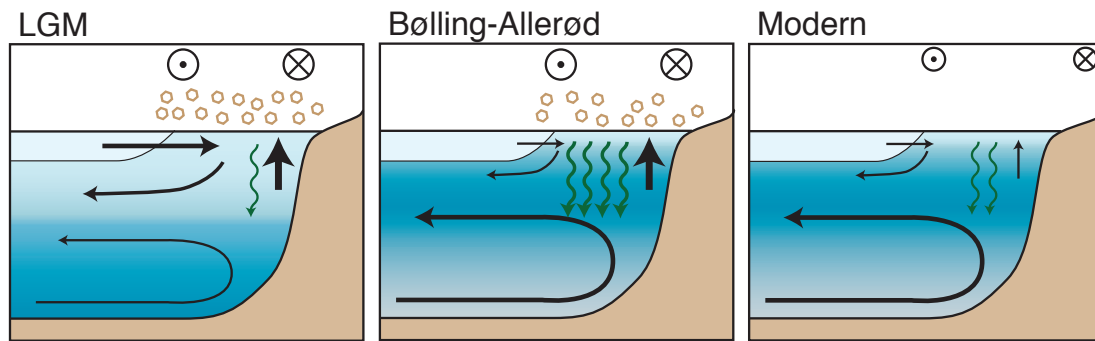
993

994

995

996

997



998

999

**Supplementary Figure 3** Schematic of circulation and upwelling (black arrows), productivity (green arrows) and atmospheric iron supply (brown symbols) during the LGM, Bølling-Allerød, and in the modern North Pacific. At the LGM, ice sheets on North America shift the easterlies south and strengthen the westerlies, driving increased Ekman suction. However, the upwelled waters have relatively low nutrient contents, due to enhanced ventilation of the upper water column by NPIW, analogous to a shallower version of the modern North Atlantic. During the Bølling-Allerød warming NPIW collapses, increasing the nutrient content of subsurface waters. The continued presence of ice on North America maintains high Ekman upwelling, driving a high flux of nutrients and CO<sub>2</sub> into the surface. Relatively high iron availability from dust, along with reduced light limitation due to seasonal stratification, also contribute to high export productivity, but are not its primary cause. The linked combination of reduced ventilation and high productivity drives hypoxia at intermediate depths.

1011

1012

1013

1014

1015

1016

1017

1018

1019

1020

1021

1022

1023

1024

1025

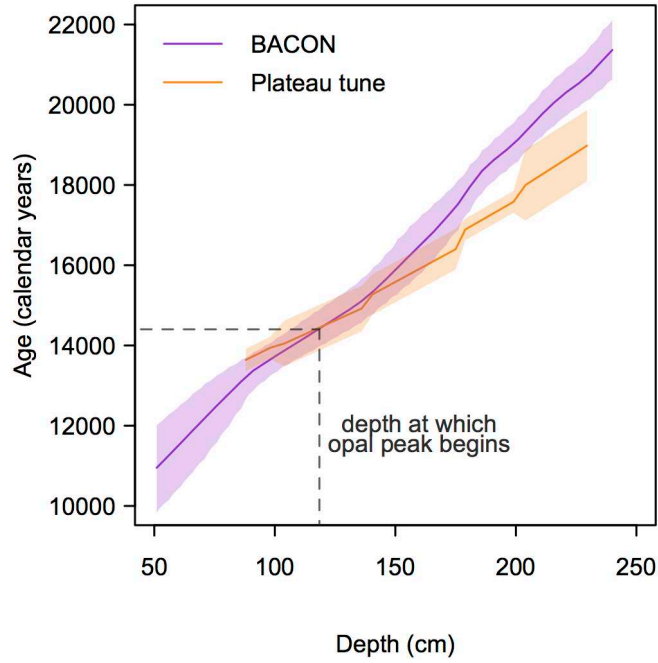
1026

1027

1028

1029

1030



1031

1032 **Supplementary Figure 4** New age model used in this study (purple), and previously

1033 published plateau-tuned age model of ref<sup>47</sup>.

1034

1035

1036

1037

1038

1039

1040

1041

1042

1043

1044

1045

1046

1047

1048

1049

1050

1051

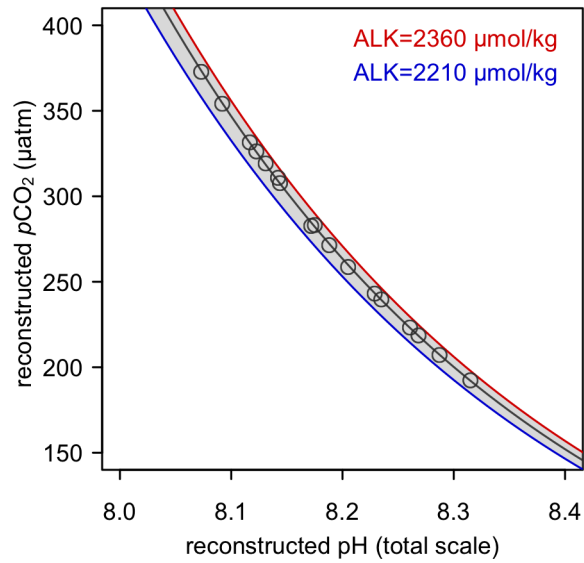
1052

1053

1054

1055

1056



1057

1058 **Supplementary Figure 5** Reconstructed  $p\text{CO}_2$  as a function of reconstructed pH with varying  
 1059 alkalinity. The range in alkalinity represented by the shaded area is equivalent to the range in  
 1060 alkalinity found within the surface of the open Pacific Ocean today<sup>15</sup>.

1061

1062

1063

1064

1065

1066

1067

1068

1069

1070

1071

1072

1073

1074

1075

1076

1077

1078

1079

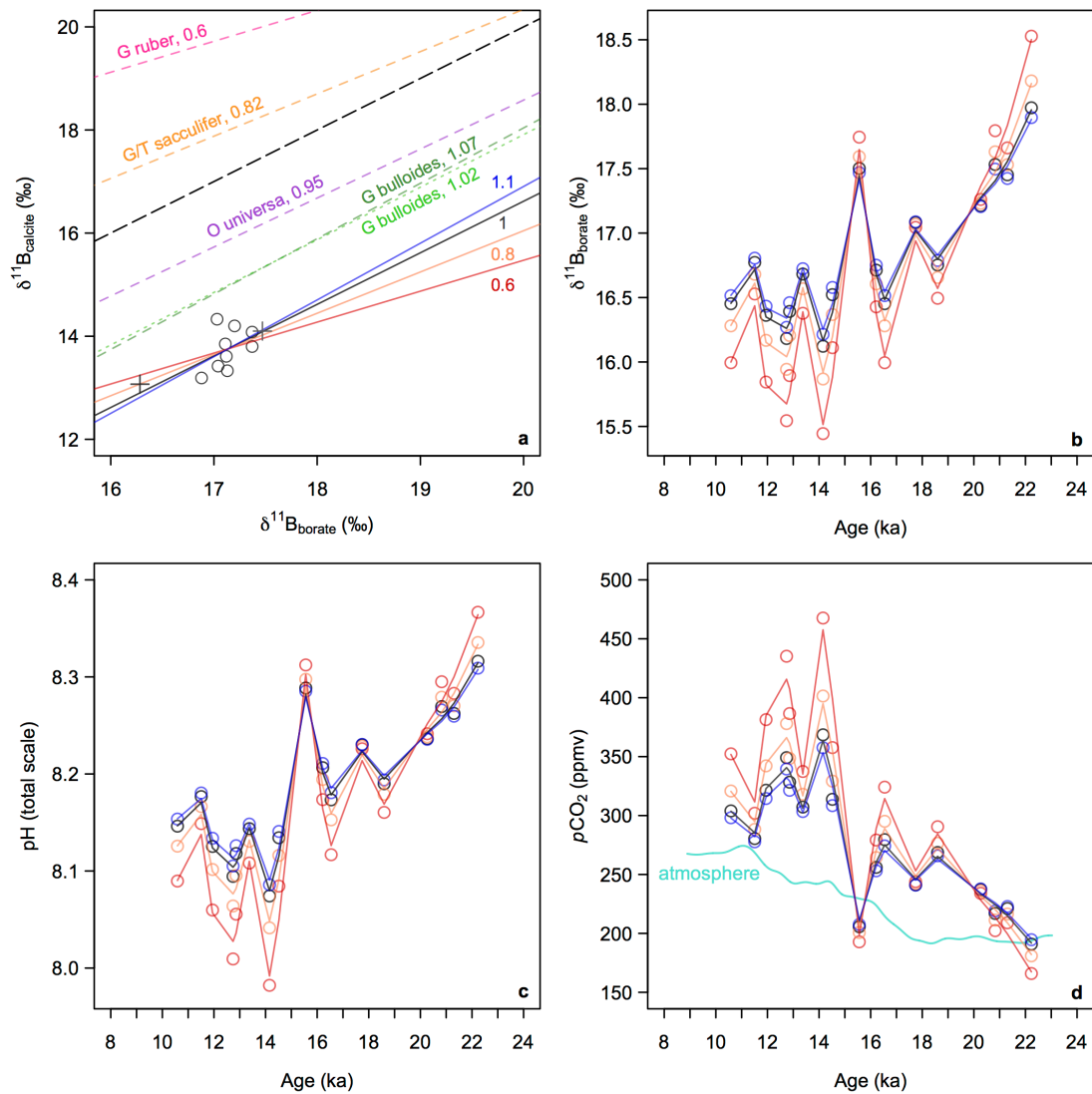
1080

1081

1082

1083

1084



1085

1086

1087

1088

1089

1090

1091

1092

1093

1094

1095

1096

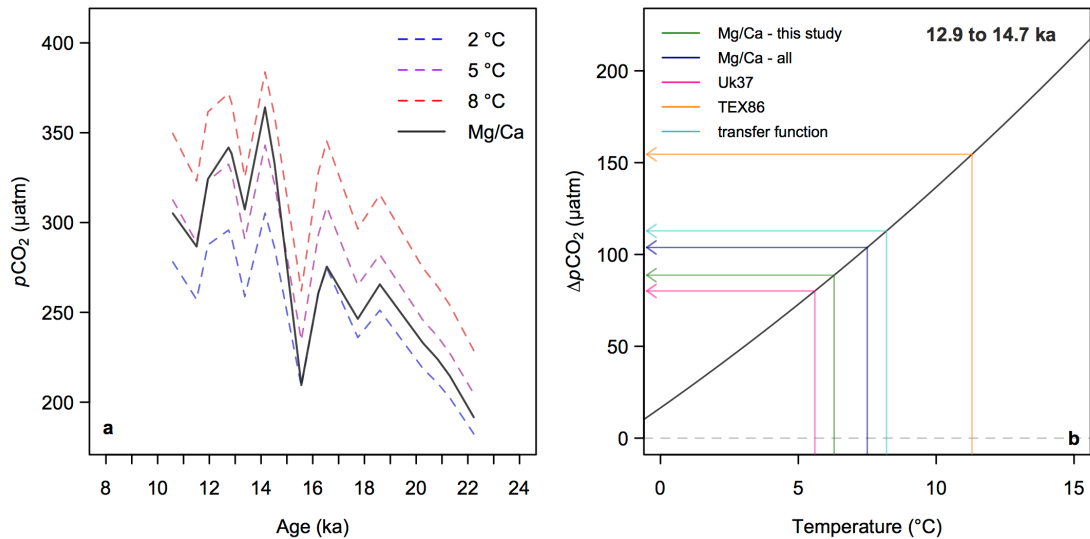
1097

1098

1099

1100

**Supplementary Figure 6**  $\delta^{11}\text{B}_{\text{calcite}}-\delta^{11}\text{B}_{\text{borate}}$  calibration sensitivity test **(a)** the dashed lines show all previously published planktic foraminiferal relationships between  $\delta^{11}\text{B}_{\text{borate}}$  and  $\delta^{11}\text{B}_{\text{calcite}}$  (refs<sup>18,65,66</sup>) with the slope of the relationship indicated. The 1:1 line is shown by the dashed black line. *N. pachyderma* coretop data of ref<sup>65</sup> are shown by the open circles. To test the sensitivity of our results to the assumed slope of the calibration line we re-calibrated the coretop data of ref<sup>65</sup>, forcing the slope of the line within the range previously observed in all other species of planktic foraminifera (0.6 to 1.1, solid lines), and allowing the intercept to vary. Newly generated Holocene  $\delta^{11}\text{B}_{\text{Npachyderma}}$  from MD01-2416 (dark-grey cross) and MD02-2489 (light-grey cross; 54.39°N, 148.92°E, 3640 m water depth) plotted against pre-industrial  $\delta^{11}\text{B}_{\text{borate}}$ , show very good agreement with the calibration proposed by ref<sup>65</sup> used in this study **(b)** down core  $\delta^{11}\text{B}_{\text{borate}}$  **(c)** pH and **(d)**  $p\text{CO}_2$  versus age (with LOESS smooth), assuming different slopes in relationship between  $\delta^{11}\text{B}_{\text{calcite}}$  and  $\delta^{11}\text{B}_{\text{borate}}$  (see panel a). This exercise demonstrates that within the range in slope previously observed in all other species of planktic foraminifera, the assumed slope of the  $\delta^{11}\text{B}_{\text{calcite}}-\delta^{11}\text{B}_{\text{borate}}$  calibration makes no difference to any of the conclusions drawn in this study.



1101

1102 **Supplementary Figure 7** Temperature-carbonate system sensitivity tests **(a)** reconstructed  
 1103  $p\text{CO}_2$  versus age at different temperatures (calculated at a constant salinity [33.9] and  
 1104 pressure [5 bar]). The coloured lines are calculated assuming a constant temperature of 2 °C,  
 1105 5 °C and 8 °C, and the black line shows pH calculated using the Mg/Ca temperatures **(b)**  
 1106 average reconstructed ocean-atmosphere  $p\text{CO}_2$  difference ( $\Delta p\text{CO}_2$ ) during the Bølling-Allerød  
 1107 (12.9 to 14.7 ka) as a function of temperature (using a salinity of 33.9 and pressure of 5 bar).  
 1108 Coloured lines show reconstructed temperature within the western subpolar North Pacific  
 1109 during this interval from all available proxy data (refs<sup>21,80-82</sup>). The temperatures suggested by  
 1110 all proxies suggest a substantial outgassing of  $\text{CO}_2$  to the atmosphere during the Bølling-  
 1111 Allerød.

1112

1113

1114

1115

1116

1117

1118

1119

1120

1121

1122

1123

1124

1125

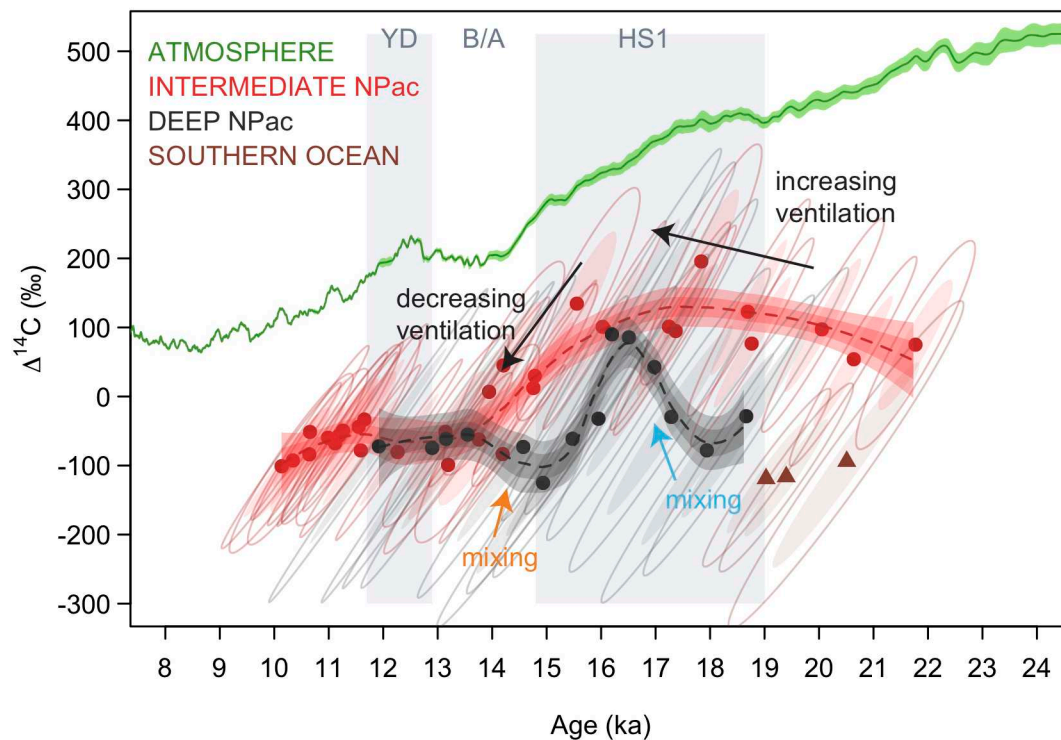
1126

1127

1128

1129





1131

1132 **Supplementary Figure 8** Benthic  $\Delta^{14}\text{C}$  records from the intermediate (<1500m) western  
 1133 North Pacific<sup>30</sup> (red circles, see caption of Figure 3 for core details) and deep North Pacific<sup>35,47</sup>  
 1134 (black circles), with the atmospheric record of ref<sup>48</sup> (green), and the LGM Southern Ocean  
 1135 data of ref<sup>S1</sup> (brown triangles). Confidence intervals are 95% (open circles) and 67% (filled  
 1136 circles). LOESS smooth shown by the dashed line with 67% and 95% confidence intervals.  
 1137 An increase in North Pacific overturning circulation is suggested during early deglaciation by  
 1138 increasing  $\Delta^{14}\text{C}$ , with deepwater formation in HS1 resulting in mixing throughout the water  
 1139 column to ~3600m (blue arrow). A reduction in intermediate water formation during the  
 1140 Bølling-Allerød results in old, radiocarbon depleted, deepwaters mixing throughout the water  
 1141 column, and low  $\Delta^{14}\text{C}$  values at intermediate depths (orange arrow). The Southern Ocean  
 1142 record of ref<sup>S1</sup> is thought to represent southern sourced deepwater, which flows into the deep  
 1143 Pacific today, and likely during the LGM.

1144

1145

1146

1147

1148

1149

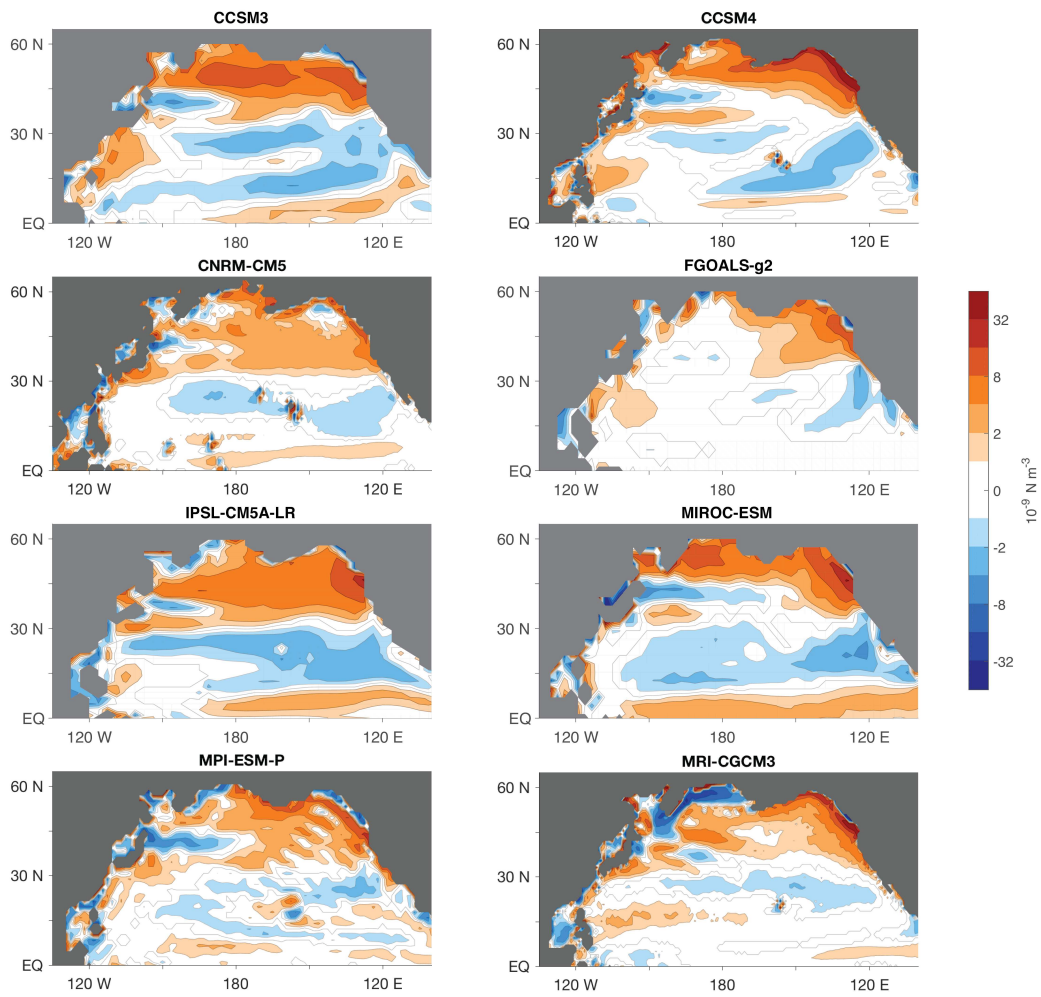
1150

1151

1152

1153

1154



1155

1156

**Supplementary Figure 9** Difference in wind stress curl within the North Pacific under glacial boundary conditions relative to pre-industrial control in PMIP3 climate model ensemble<sup>31</sup>.

1157

1158

1159

1160

1161

1162

1163

1164

1165

1166

1167

1168

1169

1170

1171

1172

**Supplementary Table 1**

The location of cores in the North Pacific from which proxy data are discussed in the manuscript

<b>Core</b>	<b>Lat (°N)</b>	<b>Lon (°E)</b>	<b>Water depth (m)</b>
RAMA-PC-44	53.00	164.65	2980
PC13	49.72	168.31	2393
ODP882	50.37	167.60	3244
SO202-07-6	51.30	167.70	2345
EW0408-85JC	59.55	-144.15	682
ODP887	54.62	-148.75	3647
ODP1017	34.53	-121.10	955
SO201-2-85KL	57.51	170.70	968
SO178-13-6	52.73	144.71	713
CH84-14	41.73	142.55	978
GH02-1030	42.23	144.21	1212
MR01K03-PC4/PC5	41.12	142.40	1366

1174

1175

1176 *Supplementary References*

1177 S1. Skinner, L., Fallon, S., Waelbroeck, C., Michel, E. & Barker, S. Ventilation of the Deep  
 1178 Southern Ocean and Deglacial CO<sub>2</sub> Rise. *Science* **328**, 1147–1151 (2010).

1179

1180